Department of Precision and Microsystems Engineering

Scoliosis Brace Design: Utilizing Compliant Shell Mechanisms and Primary Compliance Vector Path Optimization

Hylke Kooistra

Report no : 2019.014
Coach : Werner W.P.J. van de Sande
Professor : Just L. Herder
Specialisation : Mechatronic System Design
Type of report : Master Thesis
Date : 26 April 2019

Scoliosis Brace Design

Utilizing Compliant Shell Mechanisms and Primary Compliance Vector Path Optimization

by

Hylke Kooistra

to obtain the degree of Master of Science
at the Delft University of Technology,
to be defended publicly on Friday April 26, 2019 at 10:00 AM.

Student number:	4303660	
Project duration:	February 21, 2018 – April 26, 2019	
Thesis committee:	Prof. dr. ir. J. L. Herder,	TU Delft, Chair
	Ir. W. W. P. J. van de Sande,	TU Delft, Supervisor
	Assoc. prof. dr. ir. M. Langelaar,	TU Delft
	Assoc. prof. dr. MSc.Eng. C. J. Kim,	Bucknell University

An electronic version of this thesis is available at http://repository.tudelft.nl/.

TU Delft

Preface

In front of you lies the thesis that concludes my master High-Tech Engineering at Delft University of Technology, at the faculty of Mechanical, Maritime and Materials Engineering. I am honored with the outcomes of this thesis, they surpass my own expectations.

I wish to sincerely thank Charles, my advisor, for his enthusiasm and involvement during my research. I am thankful that I could visit him at Bucknell University. I would like to thank Werner, my daily advisor, for the motivating feedback and excellent guidance. I would also like to thank Just, my chair, for his critical eye and oversight.

Last, but certainly not least, I wish to thank my family and friends for their support during my thesis and studies.

Hylke Kooistra
Delft, April 2019

Contents

1 Introduction

1.1. Scoliosis Brace

Scoliosis is a 3-dimensional deformation of the human spine. The spine is not supposed to deviate in the lateral direction, the shoulder to shoulder direction. Figure 1.1 illustrates the difference between a healthy spine, C-shape scoliosis, and S-shape scoliosis.

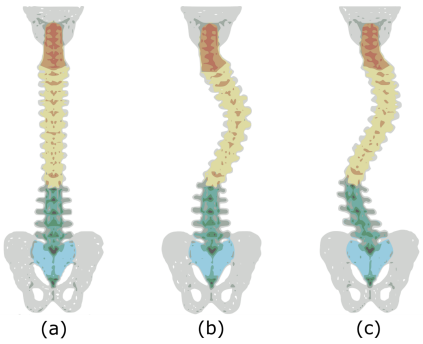

Figure 1.1: (a) Visual comparison between a healthy spine, (b) C-shape scoliosis, and (c) S-shape scoliosis [1]

Around 3% of the adolescents develop idiopathic scoliosis, a deformation of the spine without a known cause. This deformation might result in physical complications, like heart and lung problems [2]. It can also negatively affect the emotional well-being of a scoliosis patient [3]. Patients suffering from progressive idiopathic scoliosis need treatment. Mostly, a brace can inhibit that progression [4, 5]. Treatment success of a scoliosis brace relates strongly to the willingness of a patient to wear the brace [5].

The predominantly prescribed Boston brace is formed out of a copolymer plastic and lined with an aliplast for comfort [6]. This brace prevents spinal curve progression and needs to be worn until the adolescent's spine is fully developed. While inhabiting curve progression, the brace also precludes the required spinal movement for activities of daily living (ADL). Which reduces the willingness to wear the brace, thus reduces treatment success. Multiple efforts have been made in overcoming this shortcoming of the Boston brace, like the TriAc brace [7] or ROSE [8]. But none of them could hit the sweet spot between the need for correction and patient compliance [9].

Vision

We work towards a brace that hardly effects daily life of adolescents. They should be able to wear the clothes they want and participate in the activities they want. This increases the willingness to wear the brace and treatment success. Such a brace should be slim and aesthetically appealing while providing corrective loads and retaining mobility.

Previous Work

In this thesis, we build on the work of Nijssen, Leemans, and Dries [9–11]. Dries and Leemans came up with a modified version of the Boston brace. Their brace is divided into three parts. The top and bottom part apply loads to the torso. The isolated segment transmits loads between these two parts and does not interact with the torso. It expresses the mobility problem solely as a mechanical problem, which simplifies the bracing versus mobility problem.

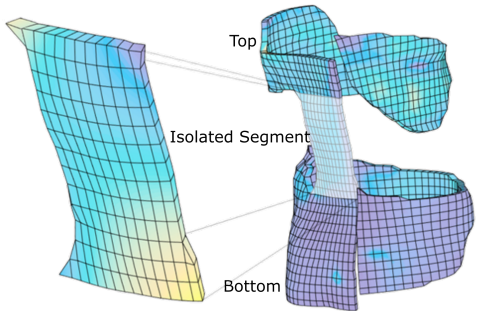

Figure 1.2: Visualization of a scoliosis brace and the isolated segment [9, 11]

Objective

The design objective in this thesis is:

Replace the isolated segment in the brace of Dries and Leemans with a passive 1 DOF mechanism that aligns with the sagittal bending axis during bending, and is aesthetically appealing.

From Nijenbanning's work and the design requirements by Dries and Leemans follows that the predominant corrective forces and moments are in the lateral plane, shoulder to shoulder direction [7, 9, 11]. These forces have to be transmitted by the mechanism that replaces the isolated segment. Bible's work shows a relatively small twist requirement (rotation around the vertical axis) and a sagittal bending requirement of 50 degrees for ADL (bending forward) [12]. The ADL and correction requirements suggest a 1 DOF mechanism.

The brace forms a closed kinematic chain with the human spine. Over-constraining should be prevented to allow for motion and prevent uncomfortable loads on the torso. Thus, the rotational axis of the brace should align with the sagittal bending axis of the spine during the entire range of motion.

1.2. Shell Mechanism Design

Shell mechanisms are spatially curved thin-walled structures and they are able to transfer or transmit force, motion, or energy through elastic deformation [13]. So, they can be used as a mechanism that provides corrective loads in certain directions and retains mobility in other directions. Their spatially curved geometry makes them more aesthetically appealing and easier to form around a human body. Furthermore, the parameters that describe the geometry can be used to tune large deformation behavior.

However, designing with shell mechanisms is challenging. Existing design methods are optimization based [13], or building block based [14]. Optimization does consider large deformation but leaves little room for designer influence. The building block method solely focuses on the initial un-deformed state.

Vision

We prefer a two-stage design method for shell mechanism design. The first stage should generate a conceptual design that nearly meets kinematic requirements. The designer should have a significant influence during this stage. The second stage should generate a detailed design that satisfies large deformation kinematic requirements. In other words, the second stage makes sure that the bending axis of the human spine and mechanism align for the entire range of motion.

Previous Work

Leemans presented a unified stiffness characterization and utilized it to compose a characterized shell mechanism building block library [15]. The characterization allows to compare rotational and translational compliances. It orders compliance vectors as freedom and constraint directions based on the compliance in that direction. The primary compliance vector (PCV) is a generalized 6-vector representing a screw. This vector indicates the direction and location of the DOF axis with the largest unified compliance. The number of degrees of freedom depends on the ratio between unified compliances.

Objective

The research objective in this thesis is:

Develop a shape optimization framework that tunes large deformation kinematic behavior, by optimizing the path of the primary compliance vector, through refinement of mechanism geometry.

The stiffness matrix of a mechanism changes as the deformation increases, thus the location of the PCV also changes. Together these locations form the PCV path. That makes it a measure for large deformation behavior. Furthermore, a PCV path objective relates easily to the mobility of human joints.

1.3. Thesis Outline

Figure 1.3 illustrates the outline and scope of this thesis. The second chapter addresses the design objective, it presents a 1 DOF compliant shell mechanism that circumscribes an object. That mechanism satisfies spatial and kinematic requirements on the isolated segment. Chapter 3 experimentally validates the mobility of the conceptual design. Chapter 4 is the main contribution of this thesis, it addresses the research and design objective. First, it presents a general framework for the optimization of the PCV path of shell mechanisms. Second, it applies the framework to the conceptual design of chapter 2. Which results in a suitable scoliosis brace mechanism to replace the isolated segment. Last, we discuss the contributions of this thesis, present recommendations for future work, and draw a conclusion.

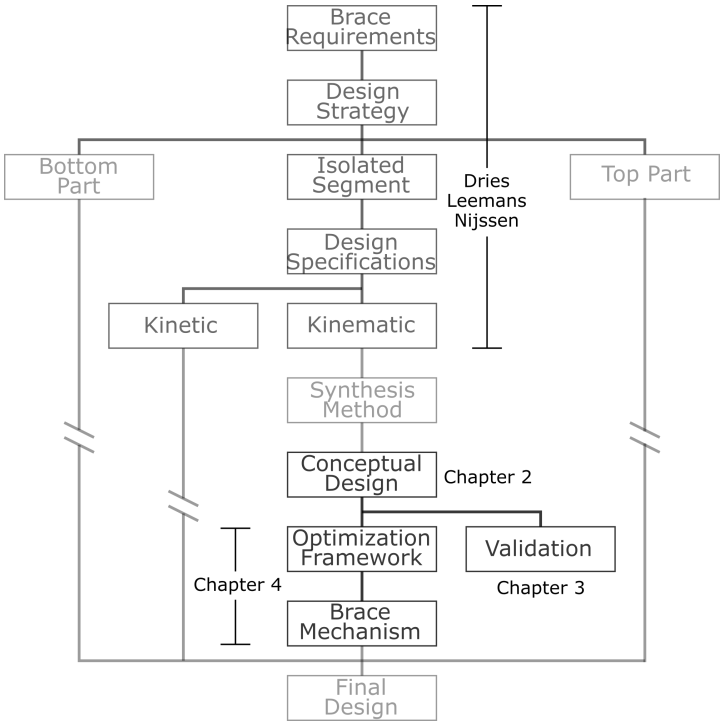

Figure 1.3: Design process, project scope, and thesis outline

2

Conceptual Design

Paper: Design of a 1 DoF Compliant Shell Mechanism that Circumscribes an Object

This paper introduces a 1 degree of freedom shell mechanism that circumscribes an object. The mechanism approximates the kinematic and geometric requirements of the isolated segment in the scoliosis brace.

Design of a 1 DoF Compliant Shell Mechanism that Circumscribes an Object

Hylke Kooistra[1], Charles J. Kim[2], Werner W.P.J. van de Sande[1], Just L. Herder[1]

[1]*Department of Precision and Microsystems Engineering, Delft University of Technology*
[2]*Department of Mechanical Engineering, Bucknell University*

Many rigid-body and compliant mechanisms exist that have 1 rotational degree of freedom. However, the hinge line of these mechanisms is located within the volume of the mechanism. Unappealing cumbersome topologies combine elements to move the mechanism away from an object. This paper presents a 1 degree of freedom shell mechanism that circumscribes an object. That mechanism can support an object while bending without the need for cumbersome topologies. Furthermore, the presented mechanism is promising for large deformation shape optimization.
The design process towards the 1 DOF mechanism starts with the characterized shell mechanism building block library. This paper highlights a limitation on the location of the bending compliance vector and uses this limitation as a selection criterion. Furthermore, the paper presents intuitive design choices to decrease sinusoidal helix mobility using serial and parallel concatenation rules. We decrease the number of revolutions and concatenate two shapes in reflective symmetry. Finally, mechanism degrees of freedom are evaluated over a large range of motion.

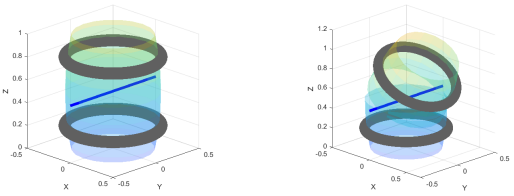

(a) Un-deformed (b) Deformed

Fig. 1: Illustration of the design objective

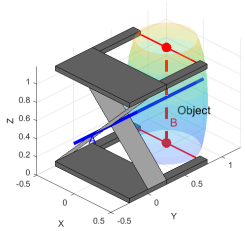

Fig. 2: Topology making use of a cross-pivot flexure and two connecting beams

1 Introduction

Compliant shell mechanisms have similar benefits over rigid-body mechanisms as compliant mechanisms. They reduce wear and backlash, making them useful in high precision environments. Furthermore, they eliminate the need for lubrication which makes them useful in all sorts of environments [1]. Shell mechanisms are spatially curved, making them aesthetically more appealing and easier to integrate into systems or tune their large deformation behavior [2, 3]. These advantages could be of great use when designing exoskeletons, or braces, or rehabilitation devices.

In this paper, we use the geometric advantage of shell mechanisms to design a mechanism that supports an object while it rotates. Figure 1 illustrates the problem, the mechanism should connect the two gray rings to support rotation around the blue line without interfering with the object. Existing solutions use cumbersome topologies to move the mechanism away from the object, see Fig. 2 for a solution that uses a cross-pivot flexure. We are looking for a mechanism that wraps around the object, that is suitable for large deformation optimization and aesthetically appealing.

Leemans characterized a library of basic shell mechanisms [4]. This library illustrates the relative degrees of freedom (DOF) of shells with compliance vectors and compliance multipliers. Compliance vectors are generalized 6-vectors representing screws [5]. From these vectors follow the direction and location of each DOF axis. Unified compliance multipliers rank the degrees of freedom. The blue line in Fig 2 represents the primary compliance vector (PCV) of the cross-pivot vector, the DOF axis with the largest compliance multiplier.

This paper uses Leemans' library as a starting point in designing the shell mechanism that circumscribes an object. It recognizes that the bending compliance vector cannot be located on the object side of the pilot points. An example of the bending compliance vector is $\mathbf{T}_{\gamma 1}$ in Fig. 3a. Pilot points are the actuated and fixed point of a mechanism, the origin and point b in Fig. 4.

Lambert summarized screw-theory based kinematic analysis by Hunt, Roth, and Waldron among others [6–11]. That summary utilizes screw-theory to describe the effect of serial and parallel links on robot mobility. Furthermore, Kim developed design rules that capture the geometric nature of compliant mechanism building block concatenation in terms of eigen-wrenches and eigen-twists, the translational and ro-

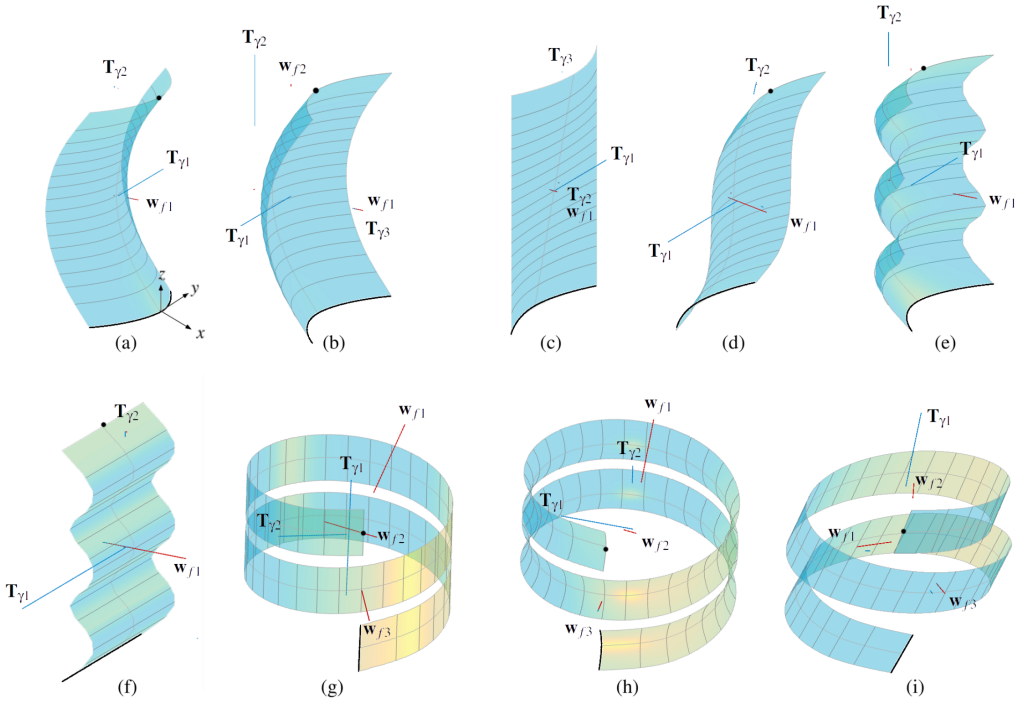

Fig. 3: Overview of the compliant shell mechanism building blocks, their unified compliances and directions in initial undeformed state [4]

tational compliance vectors respectively [12]. This paper uses the work of Lambert and Kim to support DOF decreasing design choices.

After the introduction, we elaborate on design choices in terms of the compliance vector location and degrees of freedom in the method section. Next, we present the conceptual mechanism and its DOF behavior during large deformation. Finally, we discuss the contributions of this paper and draw a conclusion.

2 Method

In this section, we present the process that generates a 1 DOF shell mechanism that circumscribes an object, is aesthetically appealing and is promising for large deformation optimization. Leemans' characterized shell mechanism building block library serves as the starting point, Fig. 3 shows the available building blocks [4]. First, we argue the need for a helix type building block and the selection of the sinusoidal helix. Next, we discuss why the number of revolutions should be reduced, and the effect of reflective symmetry concatenation.

In terms of design requirements, we are looking for a mechanism that:

- Has 1 rotational degree of freedom,
- supports rotation around an axis that intersects with the object,
- is aesthetically appealing, and
- provides geometric parameters for large deformation optimization.

2.1 Design Choice 1: Helical Building Block

For a non-helical building block, like Fig. 3a - 3f, to align the rotation axis without a cumbersome topology, the bending compliance vector should be located at the object side of the pilot points. That is not possible, thus a helical building block is needed to solve the objective. The remainder of this subsection explains why the bending compliance vector of non-helical building blocks cannot be located at the object side of the pilot points in Fig. 4. The bending compliance vector is the out of paper eigen-twist. Pilot points are the origin and point b in Fig. 4.

We investigate the location of the bending compliance vector, which is an eigen-twist, of the building blocks by modeling spinal curvature as a serial concatenation of two identical elements under an angle, see element A and B in Fig. 4. The compliance of these individual elements is described by their own compliance vectors. We assume that the bending compliance vector of these elements satisfies the following conditions:

- The unified compliance multipliers and in-element location vectors are equal, (Eqn. 2 and 4)
- individual bending compliance vectors are aligned (Eqn. 3),
- pitch is equal to zero (Eqn. 5), and
- individual eigen-twists are located on the black lines of Fig. 4 (Eqn. 6).

Element geometries that satisfy these conditions have a symmetric cross-section. They can have cross-sectional and/or spinal curvature. Thus, the modeling applies to all

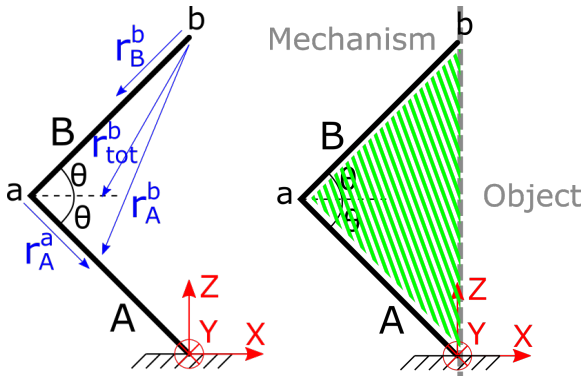

(a) (b)

Fig. 4: Definitions

non-helical building blocks in the library. Because we look at the compliance vectors, we can ignore geometric effects in the remainder of this subsection.

To show that the geometric parameters cannot locate the bending compliance vector on the object side of the pilot points, we have to show that the total location vector indicates a location within the green area of Fig. 4b for any spinal curvature. Equation 1 formulates the restriction on the location vector of the total bending compliance vector relative to point b. It states that this vector should point to a location with a negative x-coordinate within the black lines of Fig. 4. Those lines are formulated as a function of spinal curvature (θ). The z-axis coincides with the line between pilot points.

Show that:

$$\begin{bmatrix} -\ell\cos\theta \\ 0 \\ \tan\theta * x - 2\ell\sin\theta \end{bmatrix} \leq r^b_{tot} \leq \begin{bmatrix} 0 \\ 0 \\ -\tan\theta * x \end{bmatrix} \tag{1}$$

While:

$$a_A = a_B \tag{2}$$
$$\rho_A = \rho_B \tag{3}$$
$$r^a_A = r^b_B \tag{4}$$
$$h = 0 \tag{5}$$
$$\begin{bmatrix} -\ell\cos\theta \\ 0 \\ \tan\theta * x \end{bmatrix} \leq r^b_B \leq \begin{bmatrix} 0 \\ 0 \\ \tan\theta * x \end{bmatrix} \tag{6}$$

Where: ℓ is equal to the length of one element, a represents a unified compliance multiplier, ρ is the direction vector of a compliance vector, h is pitch, and r^b_B is in-element location vector of element B relative to point b. For a blade flexure element: $r^b_B = [\ -\frac{\ell}{2}\cos(\theta)\ \ 0\ \ -\frac{\ell}{2}\sin(\theta)\ ]^T$.

Because of the aligned individual eigen-twist vectors, the relation for serial concatenation with aligned eigen-twists of Kim can be used to express the total eigen-twist as a function of two individual eigen-twists, see Eqn. 7 [12]. The simplification of δ_{tot} follows from equal unified compliances, Eqn. 2.

$$\hat{\mathbf{T}}^b_{tot} = \begin{bmatrix} \delta_{tot} \\ \rho_{tot} \end{bmatrix} = \begin{bmatrix} \frac{a_A\delta_A + a_B\delta_B}{a_A + a_B} \\ \rho_A \end{bmatrix} = \begin{bmatrix} \frac{1}{2}(\delta_A + \delta_B) \\ \rho_A \end{bmatrix} \tag{7}$$

Where: $\hat{\mathbf{T}}^b_{tot}$ is the eigen-twist of the modeled shell when actuated at point b, and δ represents the moment vector.

From Chasles' theorem [13] and Eqn. 5 a twist can be expressed as:

$$\hat{\mathbf{T}} = \begin{bmatrix} \delta \\ \rho \end{bmatrix} = \begin{bmatrix} r \times \rho + h\rho \\ \rho \end{bmatrix} = \begin{bmatrix} r \times \rho \\ \rho \end{bmatrix} \tag{8}$$

Thus, a expression for the total location vector follows from relating Eqn. 3, 7 and 8:

$$\frac{1}{2}(\delta_A + \delta_B) = \frac{1}{2}(r^b_A \times \rho_A + r^b_B \times \rho_B) = \frac{1}{2}(r^b_A + r^b_B) \times \rho \tag{9}$$

$$r^b_{tot} = \frac{1}{2}(r^b_A + r^b_B) \tag{10}$$

Let the in-element location vector of element B be an arbitrary in-plane vector.

$$r^a_A = r^b_B = \begin{bmatrix} \alpha \\ 0 \\ \gamma \end{bmatrix} \tag{11}$$

Where: α and γ are the x- and z-coordinate of individual bending compliance vectors relative to element endpoint. For blade flexure elements: $\alpha = -\frac{\ell}{2}\cos(\theta)$, and $\gamma = -\frac{\ell}{2}\sin(\theta)$.

Then the location vector of element A relative to point b follows form a homogeneous coordinate transformation:

$$\begin{bmatrix} r^b_A \\ 1 \end{bmatrix} = [H]\begin{bmatrix} r^b_B \\ 1 \end{bmatrix} = \begin{bmatrix} -1 & 0 & 0 & -\ell\cos\theta \\ 0 & 1 & 0 & 0 \\ 0 & 0 & 1 & -\ell\sin\theta \\ 0 & 0 & 0 & 1 \end{bmatrix}\begin{bmatrix} \alpha \\ 0 \\ \gamma \\ 1 \end{bmatrix} = \begin{bmatrix} -\alpha - \ell\cos\theta \\ 0 \\ \gamma - \ell\sin\theta \\ 1 \end{bmatrix} \tag{12}$$

Where: $[H]$ describes a reflection around the y - z plane and a translation based on spinal curvature and element length.

Substituting Eqn. 10 11 and 12, results in an expression for the total location vector as function of curvature and the arbitrary individual location vector r^b_B:

$$r^b_{tot} = \frac{1}{2}\left(\begin{bmatrix} -\alpha - \ell\cos\theta \\ 0 \\ \gamma - \ell\sin\theta \end{bmatrix} + \begin{bmatrix} \alpha \\ 0 \\ \gamma \end{bmatrix}\right) = \begin{bmatrix} -\frac{1}{2}\ell\cos\theta \\ 0 \\ \gamma - \frac{1}{2}\ell\sin\theta \end{bmatrix} \tag{13}$$

From Eqn. 6 and 11, follows that γ as function of α (x-coordinate) is:

$$\gamma = \tan\theta * \alpha \tag{14}$$

And:

$$-\ell\cos\theta \leq \alpha \leq 0 \tag{15}$$

Thus, the total location vector:

$$r^b_{tot} = \begin{bmatrix} -\frac{1}{2}\ell\cos\theta \\ 0 \\ \tan\theta * \alpha - \frac{1}{2}\ell\sin\theta \end{bmatrix} \tag{16}$$

Which components are, for the range of α, within the boundaries of Eqn. 1. For blade flexure elements: $r^b_{tot} = [\ -\frac{\ell}{2}\cos(\theta)\ \ 0\ \ -\ell\sin(\theta)\ ]^T$. The above shows that, if the elements are identical, the overall bending compliance vector is located between the in-element bending compliance vectors. Thus, non-helical building blocks cannot locate the bending compliance vector on the object side of the pilot points.

2.2 Design Choice 2: Sinusoidal Helix

The sinusoidal helix (Fig. 3h) is the most promising remaining building block. This shell has an eigen-twist in the desired direction and location ($\mathbf{T}_{\gamma_1}$). Furthermore, it has many geometric parameters that make it suitable for large deformation optimization. However, the shell has multiple degrees of freedom. The next subsections focus on reducing the number of freedom directions.

2.3 Design Choice 3: 1/2 Revolutions

Figure 5 illustrates the unified stiffness characterization of a sinusoidal helix that makes half a revolution. Reducing the number of revolutions also reduces the degrees of freedom. In Fig. 5 the three largest compliance vectors are illustrated, all eigen-twists. The secondary twist vector has the desired direction and is in the desired location.

An analogy to mobility characterization of robots implies that decreasing the number of revolutions could decrease the number of degrees of freedom. Equation 17 calculates degrees of freedom based on the twist system of a mechanism. It calculates the maximum number of independent screws in S [6].

$$M = dim(S) \tag{17}$$

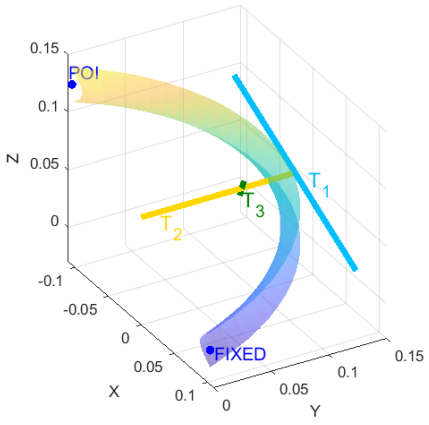

Fig. 5: Compliance vectors of a sinusoidal helix for $0 \leq u \leq \pi$

Twist system S_i of a serial chain follows from Eqn. 18 [6, 9]. It calculates the twist system between the two end links by summing the individual systems.

$$S_i = \sum_{j=1}^{q} S_{ij} \tag{18}$$

Where: i indicates the independent chain and q the number of joints.

Adding a joint to a serial chain can increase the mobility if that joint adds an independent screw to the total twist system. It cannot decrease the number of independent screws, thus it cannot add a constraint. This suggests that removing a joint from a serial chain can remove a DOF if that joint is responsible for one of the independent screws in the twist system. Otherwise, removing a joint won't have an effect on mobility.

This statement applies to rigid-body mechanisms, which have deterministic freedom directions. Compliant shell mechanisms have relative degrees of freedom, meaning: *The motion tendency of a mechanism in 3D space, defined by the relationship between the three rotational and three translational compliances* [14]. Thus, shell mechanisms have 6 independent screws but certain motions require more effort. Furthermore, the compliance vector of a shell can be relocated by a change in geometry.

Therefore, this statement is not conclusive. It suggests that decreasing the number of revolutions might yield a promising solution. The results of the unified stiffness characterization in Fig. 5 and unified compliance ratios in Eqn. 19 and Eqn. 20 confirm that suggestion. Equation 19 presents the unified compliance ratios belonging to two revolutions, Eqn. 20 presents the ratios belonging to half a revolution. The two revolutions sinusoidal helix is 4 DOF with a freedom threshold of 0.15, the half a revolution helix is 2 DOF. POI and fixed point of both mechanisms are forced to be in the same location by adapting the pitch value.

$$\frac{\tilde{a}_{f,i}}{\tilde{a}_{f,max}} = \begin{matrix}[0.10 & 0.067 & 0.93 & 0.22 & 1.0 & 0.23] \\ [\ w_x & w_y & w_z & T_x & T_y & T_z\ ]\end{matrix} \tag{19}$$

$$\frac{\tilde{a}_{f,i}}{\tilde{a}_{f,max}} = \begin{matrix}[0.0033 & 0.017 & 0.092 & 1.0 & 0.70 & 0.096] \\ [\ w_{xz} & w_y & w_{zx} & T_{xz} & T_y & T_{zx}\ ]\end{matrix} \tag{20}$$

2.4 Design Choice 4: Parallel Reflective Symmetry

Although the number of freedom directions is reduced, the half helix is not a 1 DOF mechanism and its PCV is in the wrong location and direction. Parallel concatenation of the shape in Fig. 5 in reflective symmetry, in the x - z plane and $y = 0$, results in the conceptual design in Fig. 6. This concatenation removes all eigen-twists except for the desired eigen-twist and meets the design requirements.

Kim's fourth design rule justifies concatenation in reflective symmetry [12]. This design rule states: *Use reflective symmetry in both parallel or serial concatenation to yield mechanisms with simplified eigen-twists and eigen-wrenches. In both parallel and series, the resultant eigen-wrenches and eigen-twists follow the symmetry of the mechanism (i.e. two in the plane of symmetry and one orthogonal to it).* This design rule describes the effect of reflective symmetry on the location of compliance vectors, it does not state anything about the relative degrees of freedom.

Kim's first design rule states the effect of parallel concatenation on the freedom and constraint directions: *Align freedom eigen-twists and/or eigen-wrenches under parallel concatenation to preserve them as freedoms. All other (non-aligned) freedom eigen-twists/wrenches become constraints. This assumes perfect alignment of direction, pitch, and location, although there are many cases in which freedom directions are preserved when only directions of are aligned* [12].

The two design rules explain the perseverance of the secondary eigen-twist in Fig. 5. They are not conclusive on the primary and tertiary eigen-twists becoming constraint directions. However, the decrease of relative degrees of freedom makes sense according to intuitive parallel concatenation. It is unlikely that the POI can rotate around an eigen-twist that is in the direction of T_1 in Fig. 5 and located in the symmetry plane because the eigen-twist of individual shapes is located far from the symmetry plane.

3 Results

Figure 6 presents the resulting 1 degree of freedom shell mechanism that circumscribes an object together with its compliance vectors. Equations 21 to 26 describe the geometry of the shell, leaving many parameters for optimization of large deformation behavior. Each geometric equation is formulated as a function of geometric parameters and with values belonging to the shell in Fig. 6. Mechanism material is PETG with Young's modulus: 2.0 $[GPa]$, Poisson's ration 0.4, and thickness 2 $[mm]$.

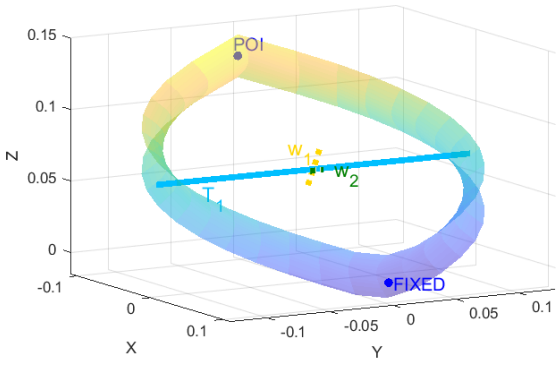

Fig. 6: Resulting mechanism with its PCV in blue

$$x(u,v) = \left(r + c\left(1 - \cos\frac{2\pi n\ v}{v_{max} - v_{min}}\right)\right)\cos u \tag{21}$$

$$= \left(0.088 + 0.055\left(1 - \cos\frac{50\pi}{3}v\right)\right)\cos u \tag{22}$$

$$y(u,v) = \left(r\ e + c\left(1 - \cos\frac{2\pi n\ v}{v_{max} - v_{min}}\right)\right)\sin u \tag{23}$$

$$= \left(0.11 + 0.055\left(1 - \cos\frac{50\pi}{3}v\right)\right)\sin u \tag{24}$$

$$z(u,v) = p\ |u| - v \tag{25}$$

$$= 0.0404\ |u| - v \tag{26}$$

Where: $-\pi \leq u \leq \pi$ and $-0.015 \leq v \leq 0.015$.

Figure 7 plots the unified compliance magnitude of the three largest compliance vectors over a rotation of 35 $[deg]$. The initial unified compliance ratios are given in Eqn. 27, indicating that rotation around the blue line is 7 times easier to perform than the second most compliant movement.

$$\frac{\tilde{a}_{f,i}}{\tilde{a}_{f,max}} = \begin{matrix}[1.0 & 0.14 & 0.025 & 0.010 & 0.0049 & 0.0] \\ [\ T_1 & w_1 & w_2 & T_2 & w_3 & T_3\ ]\end{matrix} \tag{27}$$

ANSYS APDL performed the finite element modeling. It used SHELL181 elements for the mechanism and RIGID184 elements for the boundary conditions. APDL Math incrementally extracted the global stiffness matrix and exported it to MatLab, so that the mechanism could be characterized by the unified stiffness characterization method [4].

4 Discussion

This paper introduced a 1 degree of freedom shell mechanism that circumscribes an object. The use of shell mech-

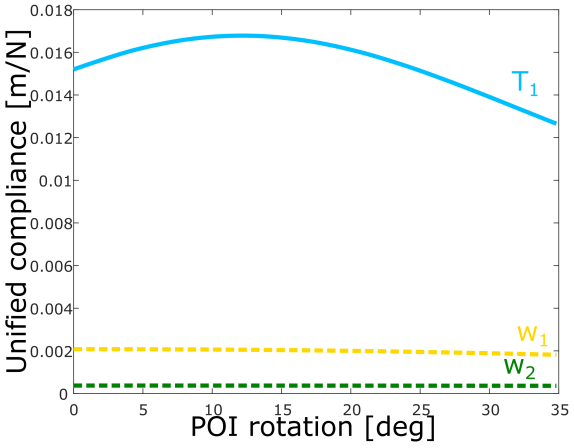

Fig. 7: Unified compliances of the first three compliance vectors over a large deformation

anisms makes the mechanism aesthetically appealing and provides many geometric parameters for optimization because the mechanism is based on the sinusoidal-helix building block. The mechanism is 1 DOF, the most compliant direction is 7 times more easy to perform than the second most compliant direction. The mechanism could perform better depending on the direction of critical correction load, the eigen-wrench or eigen-twist that should be least compliant.

The presented mechanism can be of great use in braces, exoskeletons, or rehabilitation devices. It can align with the rotational axis of a human joint, without interfering with the human body. Furthermore, successive compliance vector path optimization can align rotational axes over a large range of motion.

Second, this paper showed that curvature cannot move the bending compliance vector of a non-helix shell mechanism to the object side of the pilot points. Furthermore, the bending compliance vector can be located out of mechanism material. With that, we showed an advantage of shell mechanisms and one of their limitations. This limitation led to selecting a helix-type building block for the 1 DOF mechanism.

After selecting a building block, intelligent and intuitive design choices modified the sinusoidal-helix to be 1 DOF. These choices were supported by rigid-body kinematics and Kim's design rules [12]. They can assist with future design work, that requires relocation of compliance vectors or a decrease of degrees of freedom, but they are not conclusive.

To extract the potential of the shell mechanism building block library, a synthesis method could be developed. Such a method could address building block parameterization and concatenation. It could explain the effects on the location and direction of resulting compliance vectors and their unified compliance magnitude. This paper can function as a starting point to generate a synthesis method. Kim's work covers adding eigen-twists and eigen-wrenches in series and parallel [12].

5 Conclusion

The presented shell mechanism can circumscribe an object while supporting that object with rotation. It follows from the shell mechanism building block library. The degree of freedom properties were analyzed with the unified stiffness characterization. The mechanism is aesthetically appealing and promising for large deformation optimization.

The bending compliance vector of a non-helical shell mechanism building blocks cannot be located at the object side of the pilot points by geometric parameters. This limitation on shell mechanism building blocks helps in designing shell mechanisms and formulates a selection criterion on the characterized shell mechanism building block library.

Decreasing the number of revolutions of a helix and parallel concatenation could decrease the mobility of a shell mechanism. These choices are supported by rigid-body kinematics and Kim's design rules, but they are not conclusive.

Acknowledgements

The writers would like to acknowledge NSF No. IIS-1527133 as well as NWO-TTW (HTSM-2012 12814: ShellMech) for the financial support of this project.

References

[1] Howell, L. L., 2013. *Handbook of Compliant Mechanisms*. John Wiley & Sons.

[2] Seffen, K. A., 2012. "Compliant shell mechanisms". *Philosophical Transactions of the Royal Society A: Mathematical, Physical and Engineering Sciences,* ***370***(1965), mar, pp. 2010–2026.

[3] Radaelli, G., and Herder, J., 2017. "Gravity balanced compliant shell mechanisms". *International Journal of Solids and Structures,* ***118-119***, jul, pp. 78–88.

[4] Leemans, J., Kim, C., van de Sande, W., and Herder, J., 2018. "Unified stiffness characterization of non-linear compliant shell mechanisms". *J. Mechanisms Robotics.*

[5] Lipkin, H., and Patterson, T., 1992. "Geometrical properties of modelled robot elasticity: Part i - decomposition". In Volume 45: Robotics, Spatial Mechanisms and Mechanical Systems.

[6] Lambert, P., 2013. "Parallel robots with configurable platforms". PhD thesis, TU Delft.

[7] Hunt, K., 1978. *Kinematic geometry of mechanisms*. Cambridge Univ Press.

[8] Ohwovoriole, M. S., and Roth, B., 1981. "An extension of screw theory". *Journal of Mechanical Design,* ***103***(4), p. 725.

[9] Waldron, K., 1966. "The constraint analysis of mechanisms". *Journal of Mechanisms,* ***1***(2), jun, pp. 101–114.

[10] Dai, J. S., and Jones, J. R., 2001. "Interrelationship between screw systems and corresponding reciprocal systems and applications". *Mechanism and Machine Theory,* ***36***(5), may, pp. 633–651.

[11] Phillips, J., 1984. *Freedom in Machinery: Volume 1, In-*

troducing Screw Theory. Freedom in Machinery. Cambridge University Press.

[12] Kim, C. J., 2019. "On the geometry of stiffness and compliance under concatenation". In Proceedings of the ASME 2019 International Design Engineering Technical Conferences & Computers and Information in Engineering Conference IDETC/CIE 2019, ASME.

[13] Chasles, M., 1830. "Note sur les propriétés générales du système de deux corps semblables entr'eux et placés d'une manière quelconque dans l'espace; et sur le déplacement fini ou infiniment petit d'un corps solide libre". *Bulletin des Sciences Mathématiques, Férussac,* ***14***, pp. 321–26.

[14] Nijssen, J. P. A., Radaelli, G., Herder, J. L., Kim, C. J., and Ring, J. B., 2017. "Design and analysis of a shell mechanism based two-fold force controlled scoliosis brace". In Volume 5A: 41st Mechanisms and Robotics Conference, ASME.

3

Experimental Concept Validation

This chapter physically validates the mobility of the presented mechanism. It investigates the degrees of freedom during a sagittal bending motion and the suitability of the mechanism for the scoliosis brace application.

First, we discuss the experimental objective and how to evaluate this objective. Second, we discuss the physical model and the experimental set-up. Third, we present the experimental result. Finally, we discuss the results.

3.1. Experimental Design

The unified stiffness characterization validates the suitability of the mechanism. Unified stiffnesses enable comparison between translational and rotational compliances. A suitable mechanism has a sagittal bending unified compliance that is much larger than the compliances in all other directions. The experiment applies displacements and measures reactive loads in 6 directions. From this data follows a 6 by 6 stiffness matrix. Evaluating this matrix with Leemans' unified stiffness characterization results in the unified compliances and degrees of freedom [15].

The experiment incrementally obtains the stiffness matrix along the trajectory of the point of interest (POI) belonging to a sagittal bending motion. It does this by sequentially applying small pure translations and pure rotations at each evaluation point and measuring the resulting loads. The first column of the stiffness matrix follows from a pure translation in the x-direction and the measured resulting loads, see Eqn. 3.1 where the fractions are stiffnesses. Applying pure displacements and rotations in all 6 directions constructs the entire stiffness matrix at each evaluation point.

$$\begin{bmatrix} F_{xx} \\ F_{xy} \\ F_{xz} \\ T_{xrx} \\ T_{xry} \\ T_{xrz} \end{bmatrix} = \begin{bmatrix} {}^{F_{xx}}/_{dx} & \cdot & \cdot & \cdot & \cdot & \cdot \\ {}^{F_{xy}}/_{dx} & \cdot & \cdot & \cdot & \cdot & \cdot \\ {}^{F_{xz}}/_{dx} & \cdot & \cdot & \cdot & \cdot & \cdot \\ {}^{T_{xrx}}/_{dx} & \cdot & \cdot & \cdot & \cdot & \cdot \\ {}^{T_{xry}}/_{dx} & \cdot & \cdot & \cdot & \cdot & \cdot \\ {}^{T_{xrz}}/_{dx} & \cdot & \cdot & \cdot & \cdot & \cdot \end{bmatrix} \begin{bmatrix} dx \\ 0 \\ 0 \\ 0 \\ 0 \\ 0 \end{bmatrix} \tag{3.1}$$

The computational analysis determines the sagittal bending trajectory of the mechanism and the location of the evaluation points. The mechanism will be actuated along this trajectory.

In this experiment, we use Leemans' rotation as translation approach to compare rotational and translational compliances [11]. These compliances follow from the stiffness and compliance multipliers, which are obtained with Lipkin's eigen-decomposition [16].

$$K_t = \begin{bmatrix} \hat{\mathrm{w}}_f & \hat{\mathrm{w}}_\gamma \end{bmatrix} \begin{bmatrix} k_f & 0 \\ 0 & k_\gamma \end{bmatrix} \begin{bmatrix} \hat{\mathrm{w}}_f \\ \hat{\mathrm{w}}_\gamma \end{bmatrix} \tag{3.2}$$

$$C_t = \begin{bmatrix} \hat{\mathrm{T}}_f & \hat{\mathrm{T}}_\gamma \end{bmatrix} \begin{bmatrix} a_f & 0 \\ 0 & a_\gamma \end{bmatrix} \begin{bmatrix} \hat{\mathrm{T}}_f \\ \hat{\mathrm{T}}_\gamma \end{bmatrix} \tag{3.3}$$

Where: K_t and C_t are the tangent stiffness and compliance matrix, k_{fi} and α_{fi} are the translational stiffness and compliance multipliers for $i = 1..3$ in the direction of f_i, $k_{\gamma i}$ and $\alpha_{\gamma i}$ are the rotational

stiffness and compliance multipliers in the direction of γ_i. $\hat{\mathrm{w}}_{fi}$ are the eigen-wrenches and $\hat{\mathrm{T}}_{fi}$ are the, by an eigen-wrench, induced twists. $\hat{\mathrm{T}}_{\gamma i}$ are the eigen-twists and $\hat{\mathrm{w}}_{\gamma i}$ are the, by an eigen-twist, induced wrenches.

And Leemans' unification length:

$$\chi_i = \sqrt{h_i^2 + \left|\mathrm{r}_i\right|^2} \tag{3.4}$$

Where: h_i is the pitch of the eigen-twist, and r_i is the shortest vector from the point of interest (POI) on a mechanism to the line of an eigen-twist.

Resulting in the following unified compliances:

$$\tilde{\alpha}_f = \begin{bmatrix} \alpha_{f1} & \alpha_{f2} & \alpha_{f3} & \chi_1^2\alpha_{\gamma 1} & \chi_2^2\alpha_{\gamma 2} & \chi_3^2\alpha_{\gamma 3} \end{bmatrix} \tag{3.5}$$

3.2. Method

This section describes the physical model and manufacturing accuracy. It calculates the sagittal bending trajectory. And, it presents the experimental set-up and measurement uncertainty.

Physical Model

The physical model is constructed in accordance with the following geometric equations:

$$x(u,v) = \left(0.088 + 0.055\left(1 - \cos\frac{50\pi}{3}v\right)\right)\cos u \tag{3.6}$$

$$y(u,v) = \left(0.11 + 0.055\left(1 - \cos\frac{50\pi}{3}v\right)\right)\sin u \tag{3.7}$$

$$z(u,v) = \frac{0.127}{\pi}|u| - v \tag{3.8}$$

Where: $-\pi \leq u \leq \pi$ and $-0.015 \leq v \leq 0.015$. Units are meters and radians.

Figure 3.1 illustrates the physical model and the 6 parts that form it. Parts 3 and 4 bolt together to clamp parts 1 and 2. They create a continuous mechanism, enforce proper boundary conditions, and supply surface area for interfacing between measurement equipment and mechanism. The blue parts are 3D printed from polyethylene terephthalate (PET) and are assumed to be rigid because they have a solid fill. Parts 5 and 6 have similar functions and properties as parts 3 and 4.

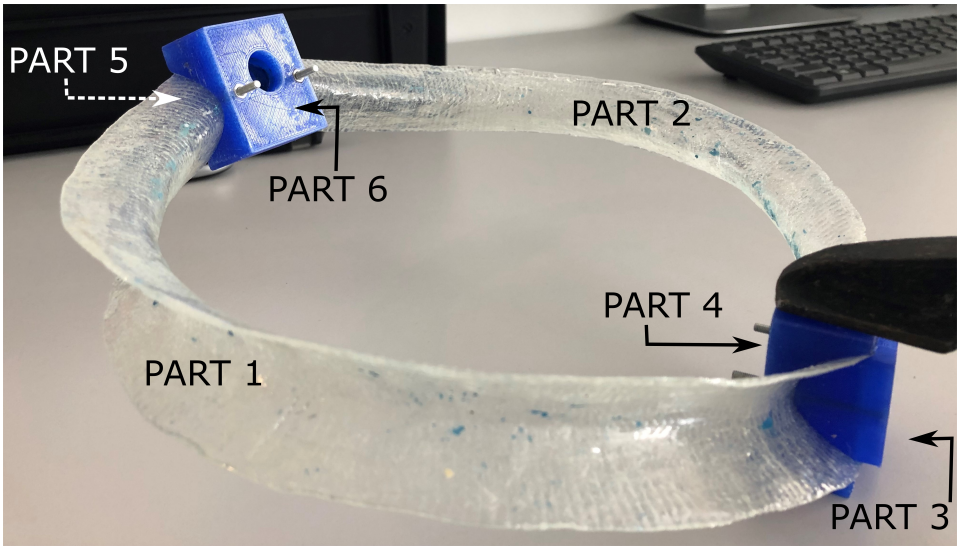

Figure 3.1: Assembled physical model

Glass fiber reinforced plastic (GFRP) forms parts 1 and 2. GFRP has the ability to form complex shapes and has high tensile strength. Aligning four unidirectional layers of fiber with a 45 degree offset ($[0 \quad -45 \quad 45 \quad 90]$) results in quasi-isotropic material properties, see Tab. 3.1. These properties are rather sensitive to deviations during manufacturing. GFRP allows for more layers of fiber than carbon fiber reinforced plastic because of the lower Young's modulus, thus allows for multiple fiber directions. A higher Young's modulus requires a thinner wall thickness to retain a certain compliance value.

Table 3.1: GFRP material properties [17]

Young's modulus	15 - 28	[GPa]
Yield strength	110 - 192	[MPa]
Poison's ratio	0.314 - 0.315	[1]

Parts 1 and 2 are formed according to a hand lay-up manufacturing process using an epoxy resin in two-sided plaster molds, see Fig. 3.2a. The molds were shaped with a 3D printed version of the mechanism, see Fig.3.2b. The fiber lay-up consists of unidirectional layers with a 45 degree offset. According to the distributor, the thickness without resin is 0.7 $[mm]$.

(a) (b)

Figure 3.2: (a) GFRP clamped between an inside and outside mold, (b) shaping the inside mold from the 3D print

Physical Model Accuracy

Table 3.2 presents the measured dimensions of the physical model. Bold font values follow from the geometric equations. Thickness measurements are performed on the long edges of the glass-fiber parts, top and bottom relate to the orientation in Fig. 3.1. Width indicates the distance between the long edges of each glass-fiber part. Amplitude is the corrugation depth of those parts. All measurements are spaced equally along the length of both glass-fiber parts. According to a tensile test, the glass-fiber Young's Modulus is 3.5 $[GPa]$ (see appendix B). The radius of the physical model in x-direction is 90.6 $[mm]$, in y-direction 110 $[mm]$, and the pitch of the model is 33.1 $[^{mm}/_{rad}]$. That is a deviation of 3.0% 0.1% and 18%, respectively.

Computational Pre-Modeling

ANSYS Mechanical APDL models the glass fiber geometry to obtain the trajectory of the point of interest (POI). This trajectory determines the location of the evaluation points, and the translation in x- and z-direction for bending around the y-axis. The model uses an average Young's modulus of 20 $[GPa]$, Poison's ratio of 0.314, and a wall thickness of 0.7 $[mm]$. Table 3.3 presents the displacements and rotation that should be applied to follow the natural sagittal bending trajectory. In other words rotation around the y-axis without constraints on the POI.

Table 3.2: Physical model accuracy

Thickness top [mm]	Thickness bottom [mm]	Width [mm]	Amplitude [mm]
0.70	**0.70**	**30.00**	**16.10**
1.13	1.00	30.95	18.66
1.16	1.24	31.23	18.57
1.45	2.00	29.98	18.18
1.16	1.24	31.30	17.10
1.16	0.92	31.35	17.22
1.03	1.18	29.84	17.66
1.38	1.74	28.60	17.76
1.66	0.89	30.27	17.12
1.06	1.64	31.52	18.55
1.08	1.34	30.78	18.20

Table 3.3: POI displacements and rotation according to ANSYS

$rot\ y\ [deg]$	$dx\ [mm]$	$dz\ [mm]$
0	0	0
2.0	2.3	3.6
4.0	4.7	7.3
6.0	7.2	10.9
8.0	9.9	14.5
10.0	12.7	18.1

Experimental Set-Up

The experimental set-up in Fig. 3.3 consists of the following components:

1. Universal Robot, UR5
2. ATI Mini40-2
3. Physical model
4. Ground

The UR5 robot moves the POI of the physical model to the desired evaluation points and induces displacement and rotation in 6 directions relative to that point. The ATI load-cell is mounted between the robot and the physical model. It measures the 6 loads applied to the physical model to achieve, by the robot induced, movements. The connection in (4) fixates the physical model to the ground. While programming the robot, the tool center point is programmed to align with the origin of the load-cell. This origin is located $11\ [mm]$ from POI of the computational model due to interfacing.

The robot applies pure displacements of $1\ [mm]$ and pure rotations of $0.5\ [deg]$. A LabVIEW program reads the measured loads from the ATI load-cell. MatLab processes these data-sets to form stiffness matrices and calculates the unified compliances. These compliances indicate the degrees of freedom along the sagittal bending trajectory.

Measurement uncertainty

According to manufacturer specifications, the UR5 robot has a repeatability accuracy of $\pm\ 0.1\ [mm]$ [18]. Table 3.4 presents the resolution and sensing ranges of the ATI load-cell [19]. Where the z-axis is orientated perpendicular to the flat surface of the load-cell.

The computational model shows minimum forces of around $1\ [N]$ in the z-direction. The induced displacements are $1\ [mm]$. From Eqn. 3.9 follows that the worst case stiffness uncertainty 10% [20]. So each component in the stiffness matrix is uncertain to 10 %.

$$\delta R = \sqrt{\frac{\delta x}{x}^2 + \frac{\delta F}{F}^2} = \sqrt{\frac{0.0001}{0.001}^2 + \frac{0.02}{1}^2} = 10.2\ \% \tag{3.9}$$

Where: δx is displacement uncertainty, δF is load uncertainty, x is displacement, and F is load.

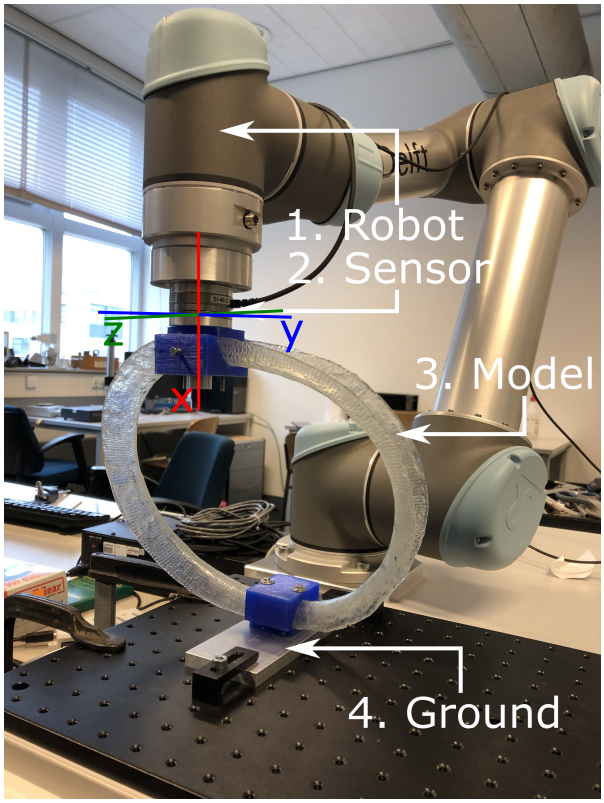

Figure 3.3: Experimental Set-Up

Table 3.4: ATI mini40-2 sensing range and resolution

Direction	Sensing range	Resolution
Fx, Fy	40 [N]	0.01 [N]
Fz	120 [N]	0.02 [N]
Tx, Ty	2 [Nm]	0.25e-3 [Nm]
Tz	2 [Nm]	0.25e-3 [Nm]

Each displacement is applied in the positive and negative direction, resulting in 3 force-displacement relations per direction. One relation based on the movement in the positive direction, one relation based on the movement between the positive and negative location, and one relation based on the returning movement.

The stiffness matrix is measured multiple times at each evaluation point. These measurements are averaged to obtain 1 stiffness matrix per evaluation point. The initial stiffness matrix is measured 10 times. At the second evaluation point, the stiffness matrix is measured 5 times. From the second to the last point, the number of measurements decreases with 1 measurement per evaluation point. Thus at 10 degrees of sagittal bending, 1 stiffness matrix is measured.

Furthermore, the resulting stiffness matrices should be symmetric thus they have 21 unique components. The experiment measures 36 components per matrix. All off-diagonal terms are averaged to obtain a symmetric and more accurate stiffness matrix.

3.3. Experimental Results

Figure 3.4 presents the unified compliance magnitudes and ratios of the physical model (Fig.3.4a and Fig. 3.4b) and of the ANSYS model (Fig. 3.4c and Fig. 3.4d). The unified compliance ratio indicates the relative degrees of freedom. It is around 20 times easier for the mechanism to perform sagittal bending compared to movements in other directions. The computed unified compliances show a smaller ratio and the sagittal bending compliance fluctuates less over 10 degrees of bending.

Unified stiffnesses follow from the stiffness matrix [15]. Force-displacement plots in appendix B

provide the data to calculate a stiffness matrix for 6 evaluation points on a sagittal bending trajectory of 10 degrees with Eqn. 3.1.

Figure 3.5 presents the translational and rotational compliance multipliers of the eigen-wrenches and eigen-twists.

Figure 3.6 shows the measured loads at the point of interest while moving the physical model along the trajectory of Tab. 3.3. Figure 3.3 indicates the coordinate system.

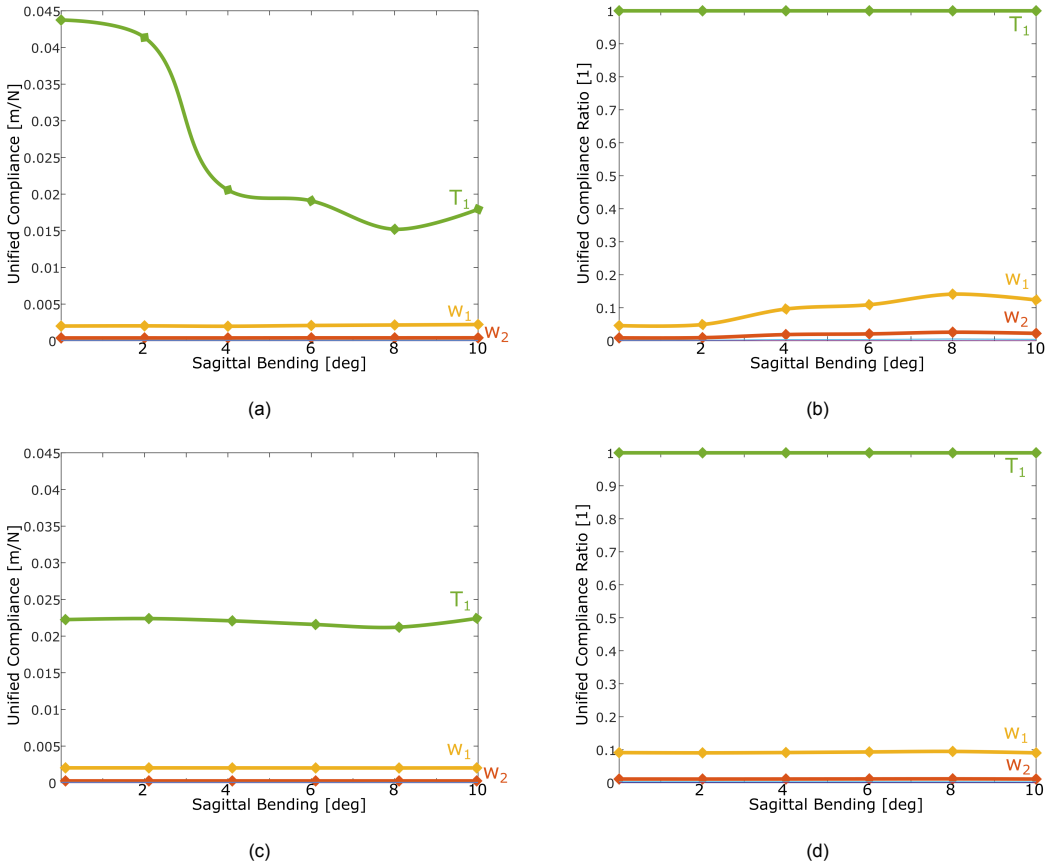

Figure 3.4: (a) Measured unified compliance, (b) Measured unified compliance ratio, (c) Modeled unified compliance, (d) Modeled unified compliance ratio

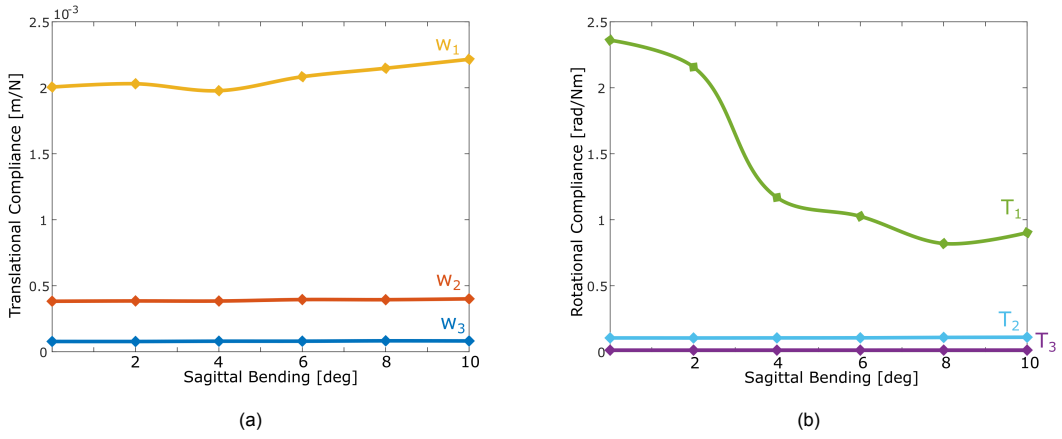

Figure 3.5: (a) Translational compliance multipliers, (b) Rotational compliance multipliers

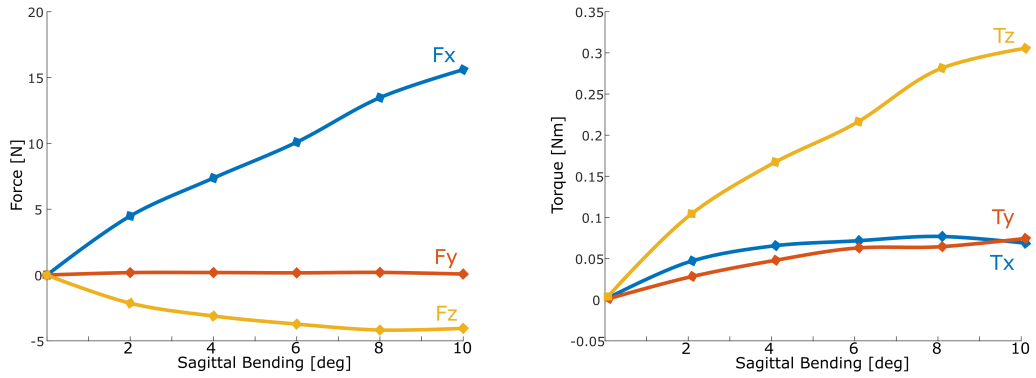

(a) (b)

Figure 3.6: Experimental force-displacement curves for 10 degrees of sagittal bending

3.4. Discussion

Unified compliance ratios in Fig. 3.4a indicate that the mechanism has one degree of freedom. It is around 20 times easier to perform sagittal bending than any other movement. Furthermore, the first critical scoliosis brace constraint direction, translation in the lateral direction, is around 100 times less compliant than sagittal bending. This makes the mechanism suitable for the scoliosis brace.

In the rotation as translation unification approach of Leemans, rotational compliance multipliers are expressed as translational compliance multipliers though a unification length [15]. The magnitude of the sagittal bending compliance could be increased or decreased by the compliance multiplier or the unification length. Figure 3.5 indicates that the difference between computational and experimental result originates in the compliance multiplier.

The difference between computational and experimental Young's modulus explains the difference between initial sagittal bending compliance magnitude. The stiffness matrix of a mechanism is the sum of a tangent stiffness matrix and a geometric stiffness matrix [10]. The tangent matrix describes kinematic characteristics in the initial and unloaded position. The geometric matrix accounts for large deformation effects. Material properties like thickness and Young's modulus show up in the tangent matrix which explains the difference between initial sagittal bending compliance magnitude.

Induced loads other than the sagittal bending torque explain the decrease of compliance compared to the computational results. Figure 3.6 indicates that loads, other than the sagittal bending torque (T_y), are present in the mechanism during deformation. Thus the applied trajectory is not equal to the natural sagittal bending trajectory. The induced loads show up in the geometric stiffness matrix, this decreases overall mechanism compliance. Which explains the decrease of the measured sagittal bending compliance. The POI shift in the measurement set-up and difference in mechanism pitch between the computational model and physical model are the likely cause of the mismatch.

Other mobility directions appear to be more sensitive to mechanism shape than material properties or internal loads, like y-translation and corrugation amplitude. A clear distinction between parameter effect could be useful when designing for robustness or for mechanism optimization.

4

Optimization Framework

Paper: Shape Optimization Framework for the Path of the Primary Compliance Vector in Compliant Shell Mechanisms

The paper presents a framework that refines shell mechanism shape to satisfy geometric and large deformation kinematic requirements. It meets these requirements by tracking the PCV path. In the paper, the framework is applied to the scoliosis brace design case. It refines the conceptual brace mechanism to meet kinematic requirements.

Appendix A includes a version of this paper that is limited to path shape optimization and contains a more simple design example. That paper is accepted by the ASME 2019 International Design Engineering Technical Conferences & Computers and Information in Engineering Conference IDETC/CIE 2019.

Shape Optimization Framework for the Path of the Primary Compliance Vector in Compliant Shell Mechanisms

Hylke Kooistra[1], Charles J. Kim[2], Werner W.P.J. van de Sande[1], Just L. Herder[1]

[1]*Department of Precision and Microsystems Engineering, Delft University of Technology*
[2]*Department of Mechanical Engineering, Bucknell University*

The primary compliance vector captures the predominant kinematic degree of freedom of a mechanism. Its displacement describes large deformation mechanism behavior and can be an optimization objective in detailed shell mechanism design. This paper presents a general framework for the optimization of the PCV path of shell mechanisms using unified stiffness characterization, Fourier descriptors, and surrogate-based optimization. We found a meaningful objective formulation for the PCV path that evaluates path shape, location, orientation, and length independently. Furthermore, we reason that design variables should effect mechanism shape. Lastly, we apply the framework to a design example.

1 Introduction

The primary compliance vector (PCV) represents the predominant kinematic degree of freedom axis of a mechanism [1]. It is a generalized 6-vector representing a screw. From this vector follows the direction and location of a degree of freedom (DOF) axis. This location changes as the mechanism is deforming. All locations combined form a path that characterizes large deformation behavior. Consider a cross-pivot-flexure, its PCV is in the direction of flexure width and initially located at half the height. Under large deformation, it moves in the direction of the actuation, that movement is comparable to axis drift [2].

Compliant shell mechanisms are a sub-category of compliant mechanisms, defined as: Spatially curved thin-walled structures able to transfer or transmit force, motion or energy through elastic deformation [3]. They have similar benefits over rigid-body mechanisms as compliant mechanisms. They reduce wear and backlash making them useful in high precision environments, or eliminating the need for lubrication making them useful in all sorts of environments [4]. Added to these benefits compliant shell mechanisms have a geometric/topological advantage over compliant mechanisms [5]. This makes them aesthetically more appealing and easier to integrate into systems or tune their large deformation behavior. These advantages could be of great use when designing exoskeletons, or braces, or rehabilitation devices.

Approaches for shell mechanism design are optimization based [3], or building block based [6]. Optimization does consider large deformation but leaves little room for designer influence. The building block method does not have this drawback but focuses solely on the initial un-deformed topology. In this work, we present an optimization framework that refines mechanism shape to satisfy large deformation kinematic requirements. It meets these requirements by tracking the PCV path. Furthermore, we explore relevant design variables.

Ullah developed a synthesis method for end-effector path generation using Fourier descriptors [7]. These descriptors characterize a path shape independent of length, orientation, and location. Rai and Mankame adapted this synthesis to make it suitable for end-effector path generation of hybrid planar path generators and compliant non-smooth path generators, respectively [8, 9]. However, there is limiting work on tracking the PCV of compliant shell mechanisms over a large range of motion.

We utilize part of Ullah, Rai, and Mankame's work for PCV path optimization of shell mechanisms. Designing for PCV path is a more fundamental design approach because one decomposition reveals force-displacement behavior and rotation-displacement relations. It is particularly useful when designing exoskeletons, braces, or rehabilitation devices.

This paper first discusses the foundation of the shape optimization framework, like mechanism characterization, path optimization, and solution method. Second, we present the framework in terms of objective function, design variables, and solution method. Third, we demonstrate the framework with a design example. Finally, we discuss the contributions of this paper and draw a conclusion.

2 Background

Mechanism optimization involves characterization, error calculation and adapting design variables. This section discusses existing knowledge in the literature on all steps of this loop. First, we elaborate on obtaining the PCV path using the unified stiffness characterization [1], this is a powerful method in analyzing the non-linear behavior of compliant mechanisms. Second, we explain the use of Fourier descriptors for path characterization [10]. Third, we discuss surrogate-based optimization.

2.1 Primary Compliance Vector (PCV)

The PCV is called an eigen-twist if the predominant DOF is a rotation, for a translation it is called an eigen-wrench. The three eigen-wrenches and eigen-twists, and their corresponding stationary stiffness or compliance multiplier values follow from Lipkin's eigen-decomposition [11].

$$K_t = \begin{bmatrix}\hat{\mathbf{w}}_f & \hat{\mathbf{w}}_\gamma\end{bmatrix} \begin{bmatrix}k_f & 0 \\ 0 & k_\gamma\end{bmatrix} \begin{bmatrix}\hat{\mathbf{w}}_f \\ \hat{\mathbf{w}}_\gamma\end{bmatrix} \tag{1}$$

$$C_t = \begin{bmatrix}\hat{\mathbf{T}}_f & \hat{\mathbf{T}}_\gamma\end{bmatrix} \begin{bmatrix}a_f & 0 \\ 0 & a_\gamma\end{bmatrix} \begin{bmatrix}\hat{\mathbf{T}}_f \\ \hat{\mathbf{T}}_\gamma\end{bmatrix} \tag{2}$$

Where: K_t and C_t are the tangent stiffness and compliance matrix, k_{fi} and α_{fi} are the translational stiffness and compliance multipliers for $i = 1..3$ in the direction of f_i, $k_{\gamma i}$ and $\alpha_{\gamma i}$ are the rotational stiffness and compliance multipliers in the direction of γ_i. $\hat{\mathbf{w}}_{fi}$ are the eigen-wrenches and $\hat{\mathbf{T}}_{fi}$ are the, by an eigen-wrench, induced twists. $\hat{\mathbf{T}}_{\gamma i}$ are the eigen-twists and $\hat{\mathbf{w}}_{\gamma i}$ are the, by an eigen-twist, induced wrenches.

The PCV is the eigen-twist or eigen-wrench with the largest unified compliance. Leemans' unified stiffness characterization enables a systematic and meaningful ordering of the rotational and translational compliances [1]. The unification variable χ_i expresses rotational compliance as equivalent translational compliance.

$$\tilde{\alpha}_f = \begin{bmatrix}\alpha_{f1} & \alpha_{f2} & \alpha_{f3} & \chi_1^2\alpha_{\gamma 1} & \chi_2^2\alpha_{\gamma 2} & \chi_3^2\alpha_{\gamma 3}\end{bmatrix} \tag{3}$$

$$\chi_i = \sqrt{h_i^2 + \left|\boldsymbol{r}_i\right|^2} \tag{4}$$

Where: h_i is the pitch of the eigen-twist, and $\boldsymbol{r}_i$ is the shortest vector from the point of interest (POI) on a mechanism to the line of an eigen-twist.

Incremental evaluation of the eigen-decomposition results in a PCV per time-step, because the stiffness matrix changes as the deformation increases. Together these vectors form the PCV path.

In contrast to end-effector behavior, the combination of PCV and compliance multipliers is an integral characterization approach. It covers force-displacement behavior and the relation between rotations and displacements.

2.2 Fourier Descriptors

In 1972 Zahn introduced Fourier descriptors and used them successfully for pattern recognition [10]. Ullah used these descriptors to compare the desired motion of an end-effector with the actual motion [7]. Rai and Mankame used this formulation for optimization based mechanism synthesis [8,9].

A Fourier descriptor objective function emphasizes the similarity in shape between paths. Consider the paths in Fig. 1 and compare the blue path to the desired red path. In Fig 1a the evaluation points are at the same location for both

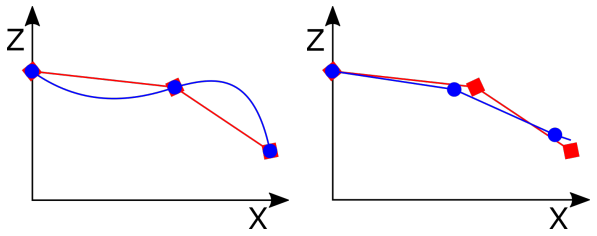

(a) (b)

Fig. 1: The desired shape in red and the actual shape in blue [9]

paths, but the shape is significantly different. A structural error objective function would suggest this solution because of the smaller point to point distance. However, Fig. 1b is a better match to the desired shape. The Fourier descriptor objective function would suggest this solution because it emphasizes shape. Furthermore, it's independent of the on-path starting point, path length, orientation, and location. On-path starting point is defined as: the location of the first evaluation point relative to the path.

The objective function can express path shape independently by comparing harmonic amplitudes and phase shifts between the desired and actual path. These descriptors follow from translating the path to a periodic step-function and expressing it as a Fourier-series. The amplitude of a step follows from the change in angle between line segments (ϕ). The time at which a step occurs follows from the normalized path length of a line segment ($\frac{\ell_i}{\ell_{end}}$). Connecting the first and last evaluation point to each-other closes the path and makes the step-function periodic because the total change in angle of one loop equals $\pm 2\pi$.

In practice, parametrization of an arbitrary path with change in angle (ϕ) and arc-length (ℓ) looks like Fig. 2a. From this parametrization follows the periodic step-function in Fig. 2b. A harmonic amplitude is the magnitude of the Fourier coefficient, phase shift is the angle of this coefficient. Fourier coefficients follow from:

$$a_k = \frac{1}{T}\int_T y(t) e^{-jk\omega_0 t} dt \tag{5}$$

Where k indicates the harmonic, $y(t)$ is the step-function, and:

$$\omega_0 = \frac{2\pi}{T} \tag{6}$$

Fourier descriptors follow from angle change and arc-length. These measures are relative to the path, making the objective independent of path orientation and location. Furthermore, arc-length is scaled so that each solution has a total arc-length of 2π, thus the objective is independent of path-length.

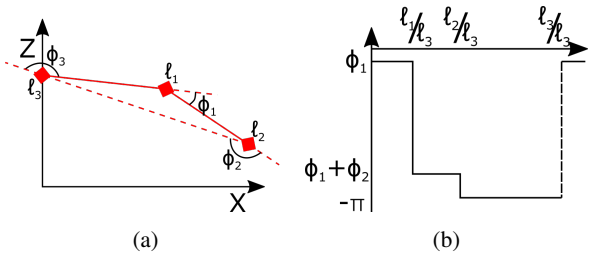

Fig. 2: An arbitrary path and the matching periodic step-function

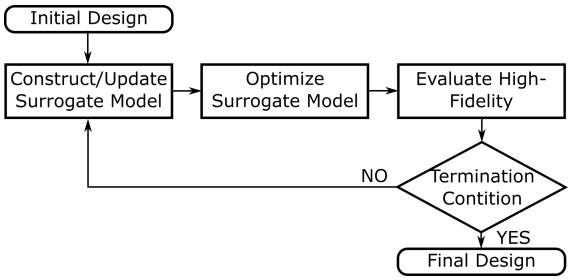

Fig. 3: Flowchart of the surrogate-based optimization process

2.3 Surrogate-Based Optimization

In surrogate-based optimization, a fast and analytically tractable surrogate model replaces a computationally expensive model [12, 13]. The optimization process comprises construction, optimization, checking, and updating of the surrogate model as illustrated by Fig. 3.

Radial basis functions construct a surrogate model based on a linear combination of multiple radially symmetric functions [12, 13]. The basis functions influence nearby points more compared to points far from the function center. Combined with weight-factors for amplitudes, the sum of basis functions replicates the high-fidelity model. Figure 4 graphically constructs a surrogate model of an objective function with exponential basis functions. The blue dots are objective values of the high-fidelity model, the red line is the surrogate. Equation 7 presents the parametric relation of this model.

$$g(\mathbf{x}) = \sum_{n=1}^{N} w_n e^{-\gamma|\mathbf{x}-\mathbf{x_n}|^2} \tag{7}$$

Where: $g(\mathbf{x})$ is the surrogate model, w_n are weight-factors determining the basis function amplitude, and $\mathbf{x_n}$ determining basis function center. γ determines the influence on nearby points, N is the number of high-fidelity data points.

The main advantage of surrogate-based optimization is the decrease in calls to the objective function [13]. Which causes a large reduction of computation time for complicated objective functions based on finite element modeling. Furthermore, it overcomes discontinuities, local minima, noise

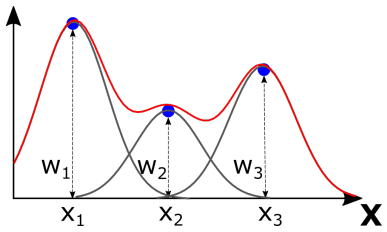

Fig. 4: Surrogate model in red of the high-fidelity model in blue, basis functions in gray

in the objective function, and it is easier to differentiate. Finally, an optimization with radial basis functions converges for a given search-space [14].

3 Framework

To optimize the PCV path of a shell mechanism, the framework should be able to deal with cumbersome FEA modeling and the designer should be able to identify key design variables. Obtaining incremental tangent stiffness matrices requires time-consuming FEA, these matrices are the source of the mechanism characterization. Furthermore, only a few design variables change the path of the PCV and affect the objective as intended.

This section describes the framework that can do the above, utilizing the presented background. This section also provides guidelines for selecting design variables. We present the framework in terms of objective formulation, design variables, mapping, and solution method.

3.1 Objective Formulation

The PCV path is the path created by the incremental PCV locations while deforming a mechanism, like the blue lines in Fig. 7. Path shape, location, orientation, and length characterize the PCV path over a large range of motion. The relative angle change ϕ_i and normalized arc-length ℓ_i characterize the shape. Location of the initial PCV it the best measure for path location. Orientation and length follow from the angle and distance between the initial PCV and the final PCV.

Rigid body transformations can meet path location and orientation requirements. However, the available design-space might limit these transformations. Therefore, the framework includes path location and orientation objectives.

The objective formulation includes path length. However, when selecting design variables that hardly influence overall compliance, path length can be left out of the objective. Adjusting thickness or mechanism length can meet the path length objective, after optimization.

3.1.1 Error formulation.

The individual error calculations are scaled so that the initial design represents baseline performance. The errors are scaled in such a way that the error of the initial design equals unity. The conceptual design approximates the desired char-

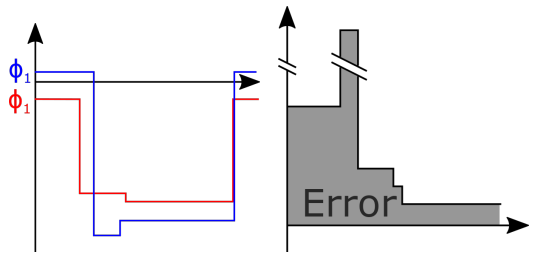

(a) (b)

Fig. 5: The shape error (in gray) between the red and blue path

acteristics, thus values of unity are reasonable for the initial design. Scaling the individual errors makes them insightful, have a similar magnitude, and makes weight-factors predominantly related to the importance of a characteristic.

Equation 8 presents the total objective function. Where: Ψ_s is path shape error, Ψ_d is location error, Ψ_θ is orientation error, Ψ_ℓ is length error, w represents the weight-factors, and subscript 1 indicates the initial error value. Squaring the individual errors penalizes designs that perform worse than the initial design quadratically and award designs that perform better.

minimize :

$$\Psi_{tot} = w_s\left(\frac{\Psi_s}{\Psi_{s_1}}\right)^2 + w_d\left(\frac{\Psi_d}{\Psi_{d_1}}\right)^2 + w_\theta\left(\frac{\Psi_\theta}{\Psi_{\theta_1}}\right)^2 + w_\ell\left(\frac{\Psi_\ell}{\Psi_{\ell_1}}\right)^2 \tag{8}$$

3.1.2 Path shape error.

A combination of step-functions represents the shape of a PCV path. Comparing the function of the actual path to the desired path results in the error value.

The error follows from taking the absolute difference between the functions and integrating that difference, see Eqn. 9. The integration interval equals the path length belonging to an angle change of 2π, after normalization this length equals unity. Figure 5 is a graphical clarification of the error between the shape of the blue and red path of Fig. 6a. The left sub-figure shows both step-functions, the right sub-figure indicates the error.

$$\Psi_s = \int_0^{\ell_{end}} ||y(t) - y^*(t)||dt \tag{9}$$

Section 3.2 describes the mapping of PCV locations to arc-length (ℓ) and step functions ($y(t)$). The asterisk indicates the desired path shape.

This error formulation is more simplistic than the Fourier descriptor error formulation. It consists of only one error term and does not have to balance the harmonic impact. A Fourier descriptor objective uses error in phase shift and amplitude to optimize shape, these metrics are co-dependent on the number of harmonics. Large harmonics usually have smaller amplitudes, thus the amplitudes of a high harmonic have less impact on the error compared to a low harmonic.

Like Fourier descriptors, the presented objective function is independent of path orientation, location, and length. However, it is dependent on the on-path starting point, because the representation of actual and desired shape is not periodic.

3.1.3 Path location error.

In most cases, rigid body translations of the mechanism can satisfy the PCV path location objective. Possible design space bounds can limit the range of rigid body translations. Equation 12 calculates the structural error between the initial primary compliance vectors of the actual and reference PCV path. With this formulation, the framework can satisfy path location while respecting design space limits.

$$\Psi_d = \sqrt{(X_1 - X_1{}^*)^2 + (Z_1 - Z_1{}^*)^2} \tag{10}$$

Where: X_1 and Z_1 follow from the mapping in section 3.2.

3.1.4 Path orientation error.

Analog to the location, design space bounds can prevent the path orientation objective from being satisfied with rigid body rotations. Equation 11 includes the orientation of the PCV path in the total objective. This equation calculates the difference in angle that the closing line segment, the dashed red line in Fig. 2a, makes with the x-axis.

$$\Psi_\theta = \left|\theta_{end} - \theta^*_{end}\right| \tag{11}$$

3.1.5 Path length error.

Error in path length follows from comparing the arc-lengths of the closing line segment between the actual path and reference path.

$$\Psi_\ell = \left|\ell_{end} - \ell^*_{end}\right| \tag{12}$$

Path length is strongly related to the displacement of the point of interest and thus the applied boundary conditions and overall compliance. For example, if a load is applied to the POI, the path length could be matched by adapting the overall compliance.

Mitigations are constraints on the minimum and/or maximum overall compliance, or expressing the desired path length as a ratio of the POI displacement, or applying a displacement loading condition. Path length can be left out of

the objective function if the design variables hardly affect overall compliance. Then, path length has to be manually tweaked during post-processing with parameters like thickness or mechanism length.

3.1.6 Conditions.

A polygon is needed for the mapping from incremental primary compliance vectors to the shape describing step-functions. For the mapping to be valid, the orientation of the PCV should not change over the deformation. Furthermore, the desired and actual PCV should be aligned. The equality constraint in Eqn. 13, which is valid for a twist PCV, introduces this condition. The next section discusses the actual mapping.

$$c_1 = \boldsymbol{\rho}(\mathbf{x})_i \cdot \boldsymbol{\rho}^* - 1 = 0 \tag{13}$$

Where: c_1 is the first equality constraint, and $\boldsymbol{\rho}$ is the PCV direction vector. The desired PCV direction ($\boldsymbol{\rho}^*$) should not change over the deformation.

3.2 Mapping

The amplitude and location of the steps in the shape describing step-function originate in the incremental stiffness matrices. Leemans' unified stiffness characterization extracts the PCV from these matrices. This section describes how to express PCV path shape as a combination of step-functions (see Eqn. 18). The mapping starts with obtaining the PCV location vector for each load-step. Equation 14 calculates the shortest vector ($\mathbf{r}$) between the POI and a twist PCV.

$$\mathbf{r} = \frac{(\boldsymbol{\delta} - h\boldsymbol{\rho}) \times \boldsymbol{\rho}}{\boldsymbol{\rho} \bullet \boldsymbol{\rho}} \tag{14}$$

Where: $\boldsymbol{\delta}$ is the moment vector of a PCV, $\boldsymbol{\rho}$ is the direction vector, and h is the pitch:

$$h = \frac{\boldsymbol{\rho} \bullet \boldsymbol{\delta}}{\boldsymbol{\rho} \bullet \boldsymbol{\rho}} \tag{15}$$

Together all PCV locations form the PCV path. This path is projected on a plane and expressed as a polygon like Tab. 1. In the table, X_i is the PCV location x-component of the i^{th} load-step, and Z_i the z-component. A similar table describes the desired path, only those values are hand-picked.

From this polygon follows the length of the line segments ($\Delta\ell_i$) and the change in angle between line segments ϕ_i. See Fig. 2 for clarification.

Table 1: Polygon data belonging to an arbitrary PCV path

load-step	1	2	...	end
X	r_{x_1}	$\Delta x_2 + r_{x_2}$	...	$\Delta x_{end} + r_{x_{end}}$
Z	r_{z_1}	$\Delta z_2 + r_{z_2}$	...	$\Delta z_{end} + r_{z_{end}}$

$$\Delta\ell_i = \sqrt{(X_{i+1} - X_i)^2 + (Z_{i+1} - Z_i)^2} \tag{16}$$

Where: X and Z follow from Tab. 1. When i is equal to the number of load-steps, the line segment length follows from replacing $(i+1)$ with 1 in Eqn. 16.

$$\phi_i = \theta_i - \theta_{i-1} = \tan^{-1}\frac{(Z_i - Z_{i-1})}{(X_i - X_{i-1})} - \tan^{-1}\frac{(Z_{i-1} - Z_{i-2})}{(X_{i-1} - X_{i-2})} \tag{17}$$

Where: θ_i is the angle between a line segment i and the positive x-axis.

Lastly, arc-length and change in orientation form the step-function that describes PCV path shape:

$$y(t) = \phi_1 + \sum_{i=2}^{n} \Delta\phi_i u(t - \tilde{\ell}_{i-1}) + (\phi_1 - \phi_{end})u(t - \tilde{\ell}_{end}) \tag{18}$$

Where $u(t)$ indicates a step function, n is the number of load-steps, and $\tilde{\ell}$ is the normalized arc-length with a periodic interval of one:

$$\tilde{\ell}_n = \frac{\sum_{i=1}^{n} \Delta\ell_i}{L} \tag{19}$$

And:

$$\Delta\phi = \phi_i - \phi_{i-1} \tag{20}$$

3.3 Design Variables

A set of design variables is valid if a change in their value has an effect on the value of the objective function, thus on the path of the primary compliance vector. Figure 6b is a graphical representation of the impact that a set of design variables should have on the PCV path. They should change the PCV path (in blue) in such a way that it matches the desired path (in red).

The tangent compliance matrix is the inverse of the tangent stiffness matrix. This matrix can be split into two matrices, the physical stiffness matrix and the geometric stiffness matrix, see Eqn. 21 for the finite element formulation of the tangent stiffness matrix of a non-linear system [15].

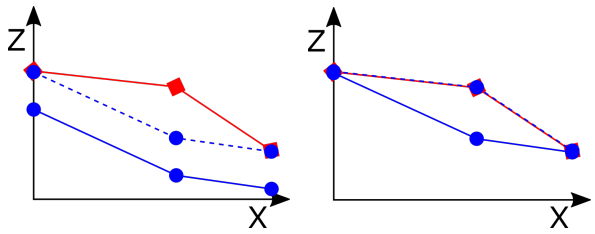

(a) Location (b) Shape

Fig. 6: The desired path in red, the actual path in blue, and the design variable effect in dashed blue

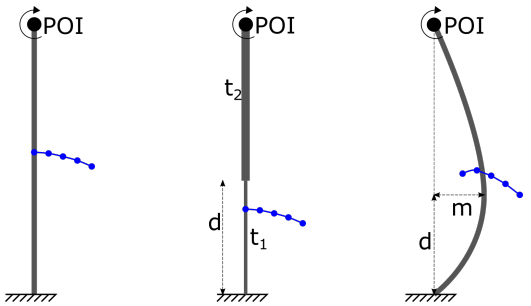

(a) (b) (c)

Fig. 7: Three flexure geometries with their PCV path in blue

$$C_t^{-1} = K_t = \int_V (B^T D B + G) dV = K_p + K_g \qquad (21)$$

Where: B is the differentiation matrix, D is the elasticity matrix which includes material properties, G is the geometric stiffness matrix which is equal to K_g, and K_p is the physical stiffness matrix. This last matrix (K_p) describes the initial un-deformed behavior. Whereas the geometric matrix is based on changing geometry and describes the non-linear behavior.

Because the compliance matrix contains all instantaneous kinematic characteristics of a compliant shell mechanism, design variables should influence the physical compliance matrix to have an effect on the initial location of the PCV (Fig. 6a). Variables to achieve this are a difference in thickness or a difference in material properties.

Effecting the path of the PCV (Fig. 6b) is more challenging. If the change between incremental geometric compliance matrices differs when changing the values of the design variables, they have an impact on the path of the PCV.

Geometric phenomena that cause path change are: Change in the second moment of area and change in mechanism length, defined as the shortest distance between the point of interest and the point of constraint [1]. Design variables that affect these phenomena are related to mechanism shape, like curvature or number of corrugations.

Figure 7 shows three flexure geometries and their, from a couple moment at the POI, resulting PCV path (in blue). In Fig. 7b difference in thickness along flexure length alters the initial geometry, t_1 and t_2 indicate thickness difference, d indicates the transition point between t_1 and t_2. These design variables change the initial location of the PCV. Path shape remains similar but could be scaled, because of overall compliance and relative mechanism length. The path shape of Fig. 7a can be reconstructed for any d if thicknesses are picked cleverly. These design variables chiefly affect the physical stiffness matrix.

In Fig. 7c curvature along flexure length alters the initial geometry, m indicates curvature amplitude and d indicates the vertical location of m. These design variables change the PCV path shape compared to Fig. 7a, without having a significant impact on overall compliance. These design variables affect the difference between incremental geometric stiffness matrices.

3.4 Solution Method

The selected solution method is the surrogate-based optimization algorithm in the Matlab Global Optimization Toolbox [16]. It is selected because of the earlier mentioned advantages.

An additional advantage is the requirement of lower and upper bounds on the design variables. These bounds help to enforce a search-space for which the finite element model converges.

A penalty objective function implements constraints, because the surrogate-based optimization algorithm does not accept constraint equations, and because the number of FEM evaluations should be kept to a minimum. If statements enforce constraint violations. If a constraint is violated, the objective is set to a large value.

4 Design Example

The design example in this section gives an indication of the use and outcome of the presented framework. First, we introduce a design case and a conceptual design. Second, we formulate the objective, followed by the parametrization and modeling of the mechanism. Finally, we present the outcome.

4.1 Case

A passive scoliosis brace that provides corrective loads while retaining patient mobility could significantly increase scoliosis bracing treatment success [17]. This new brace should have a mechanism that allows for sagittal bending, applies corrective loads to the torso, is aesthetically appealing, and comfortable.

Figure 8a presents a conceptual design that has only one relative degree of freedom, the blue twist PCV in the sagittal bending direction. The extent to which sagittal bending is allowed and brace comfort depend on the alignment of mechanism PCV and the sagittal bending axis of the spine. Proper alignment during the entire motion prevents over-constraints and uncomfortable loads on the torso.

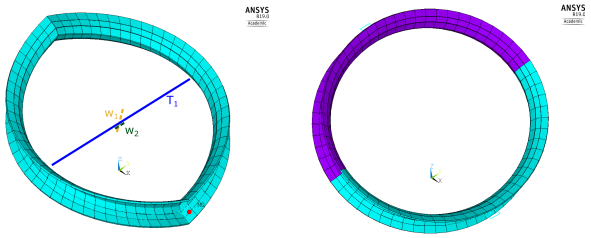

(a) (b)

Fig. 8: (a) Conceptual design with in blue the twist PCV (b) Optimized design

Table 2: Polygon data belonging to the sagittal bending axis

load-step	1	2	...	11
X^* $[m]$	0.01	0.014	...	0.04
Z^* $[m]$	0.075	0.078	...	0.094

4.2 Objective

The optimization should turn the conceptual design into a detailed design that matches the location and trajectory of the sagittal bending axis. Dries measured the spinal movement of scoliosis patients [18]. A rough estimation, based on Dries' data, results in a relation that describes the incremental locations of the sagittal bending axis during bending, see Eqn. 22. Furthermore, the axis is initially located at $x = 0.01$ $[m]$ and $z = 0.075$ $[m]$ in mechanism coordinates. Table 2 presents the reference polygon.

$$Z^*(X) = -0.03244X^2 + 0.7137X + 0.06785 \tag{22}$$

The path length that Tab. 2 indicates is arbitrary because the design is parameterized in such a way that path length can be changed after optimization and the trajectory is a close to a linear relation. Therefore, the path length error weight-factor is set to zero.

The extent to which rigid body transformations can be performed is limited because the mechanism has to circumscribe the torso. Therefore, the objective includes path orientation and location. The human spine can overcome deviations in path shape by engaging vertebrae to a different extent. Thus, path shape is rated less important than path orientation and path location. Weight-factors related to these characteristics are set to three. The path shape weight-factor is set to unity. Equation 8 presents the objective formulation.

4.3 Parametrization

Equation 23, 24, and 25 describe the conceptual design in Fig. 8a. The concept dimensions are so that it is suitable for the example scoliosis patient in Dries' work.

Table 3: Brace mechanism parameters

thickness	2±t	[mm]
E-modulus	2	[GPa]
Poisson's ratio	0.4	[1]

$$x(u,v) = \left(0.088 + 0.055\left(1 - \cos\frac{5\pi}{3}v\right)\right)\cos u \tag{23}$$

$$y(u,v) = \left(0.11 + 0.055\left(1 - \cos\frac{5pi}{3}v\right)\right)\sin u \tag{24}$$

$$z(u,v) = p\,|u| - v \tag{25}$$

Where: x, y, and z are the respective coordinates. $-\pi \leq u \leq \pi$ represents the rotation in radians, $-0.015 \leq v \leq 0.015$ represents shell width in meters, and p is the pitch in meters per radian.

Table 3 presents material properties and thickness of the mechanism. t is a thickness variation that will be discussed later on.

To be able to satisfy the total objective function, design variables should affect path location, orientation, and shape. They should influence individual characteristics without worsening other characteristics, or be able to compensate secondary effects.

Mechanism pitch strongly relates to mechanism shape. Pitch describes the inclination per rotation between the fixed point and the POI (see Fig. 9) This makes it a good parameter for optimizing path shape. Pitch does not rotate the mechanism but it has an effect on the relative orientation of the red dots in Fig. 7. It also affects path orientation and location.

To compensate secondary effects of pitch and meet the orientation objective, rotation around the Y-axis is the second a design variable (β in Fig. 7). It is formulated in such a way that the relative orientation of the pilot points is bounded by the combination of pitch and rotation. For example, a small pitch value allows for a large rotation value because these values leave enough room for a human torso between the red dots in Fig. 7. To guarantee enough room for the patient's torso, the geometric equations include rotation in such a way that the horizontal distances remain constant. This parametrization does affect mechanism length, so path length could be affected. This design variable also affects path location.

A difference in thickness between the front and back half of the mechanism ()t_1 and t_2 in Fig. 7) shifts path location along the line connecting the attachment points. A final design variable that shifts the entire mechanism in the vertical direction (d in Fig. 7) allows moving the path in 2 dimensions, in combination with the difference in thickness. Thus, it is possible to meet the path location objective.

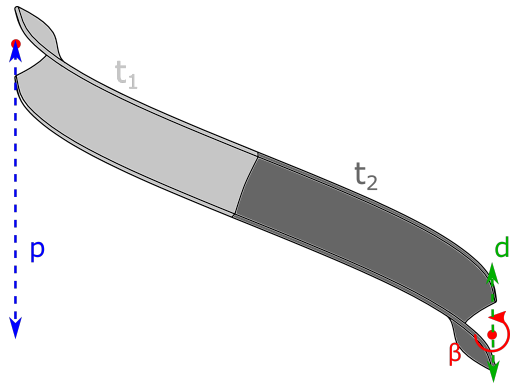

Fig. 9: Visualization of brace-mechanism design variables

Table 4: Search-space bounds

	lower-bound	upper-bound
thickness (Δt)	-1.1 $[mm]$	0.80 $[mm]$
rotation (β)	0.0 $[deg]$	50 $[deg]$
pitch (p)	-0.0200 $[^{m}/_{rad}]$	0.0404 $[^{m}/_{rad}]$
z-shift (d)	-0.10 $[m]$	0.10 $[m]$

4.4 Finite Element Modeling

ANSYS APDL performs the finite element modeling. Key-point locations, related to the design variables and calculated by Matlab, define the geometry. The key-points form an area, SHELL181 elements mesh this area.

Connecting all nodes that form the attachment edges with RIGID184 elements achieves rigidity of these respective edges. A pilot point is added to the middle of both edges, representing the fixed point and the POI. Loads and displacement constraints are applied to these points. The twist PCV over a large range of motion follows from applying a 0.75 $[Nm]$ torque on the top pilot point.

APDL Math incrementally extracts the global stiffness matrix and exports it to MatLab, so that the optimization algorithm can calculate the compliance vector path and determine new values for the design variables.

4.5 Result

Running a surrogate-based optimization as described in Sec. 3.4, with 398 iterations and a search space as indicated by Tab. 4, produces the optimized design in Fig. 8b. The purple half of the design has a thickness of 2.3 $[mm]$, the cyan half has a thickness of 1.8 $[mm]$, mechanism pitch is 0.0076 $[^{m}/_{rad}]$, rotation is 41 $[deg]$, and vertical shift is 0.0095 $[m]$.

Figure 10 gives insight into the performance of the optimized geometry. The optimized PCV path (in red) closely approaches the desired PCV path, the blue arrow indicates the desired orientation and location. The black line indicates the initial PCV path. Figure 11 presents the perpendicular

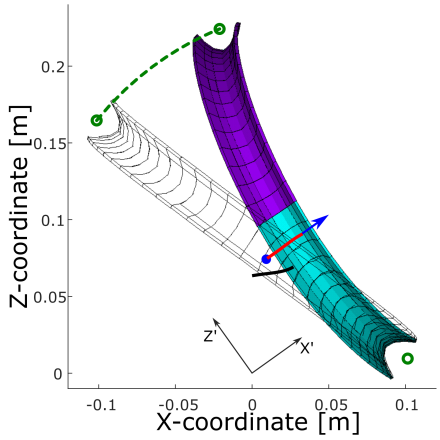

Fig. 10: Resulting PCV path in red under large deformation, desired orientation and location in blue, initial PCV path in black

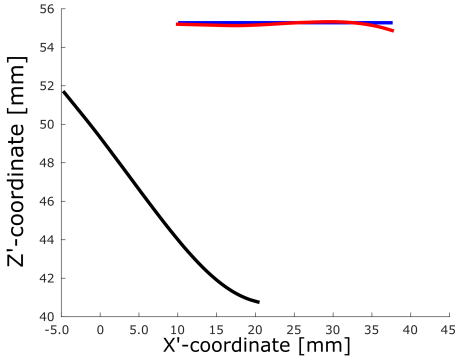

Fig. 11: Rotated close up of the desired (blue), actual PCV path (red), and PCV path of the initial design (black)

distance between the desired path and the actual PCV path. It shows that the maximum path deviation is 0.44 mm with a POI rotation of 40.5 $[deg]$. The initial PCV location is off by 0.30 $[mm]$, and the difference in orientation is 0.76 $[deg]$. The black line represents the PCV path of the conceptual design. Furthermore, Fig. 12 presents the unified compliance ratios. From these ratios follows that the mobility of the optimized mechanism did not change.

5 Discussion

The presented framework can tune large deformation behavior by optimizing the path of the PCV. The framework independently optimizes path shape, location, orientation, and length. The results of the design example in the previous section clearly show the capabilities of the framework. There is only a marginal error between desired and actual PCV path (see Fig. 11). This error is manageable for scoliosis bracing because the patient's spine can compensate for small PCV and sagittal bending axis misalignments by engaging multiple vertebrae to a different extent.

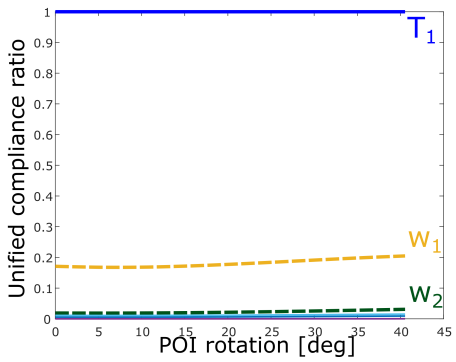

Fig. 12: Unified compliance ratios indicating the degrees of freedom

It is easy to translate design requirements to the objective formulation, especially for exoskeletons, braces, or rehabilitation devices. All these applications need to follow the rotational degree of freedom axis of a human joint, which translates directly to the PCV path.

Design variables have a significant impact on the solution-space. The set of design variables in the design example are able to achieve the objective because they affect the change in incremental stiffness matrices. If they do not affect this change, they hardly influence the shape of PCV path. Causing a limited solution-space, which is more suitable for initial location and path orientation optimization.

This framework uses Fourier-descriptor path characterization. However, it does not compare harmonic amplitudes and phase shifts in the objective. Comparing the path describing step-functions simplifies the objective. It maintains the separation between shape, location, and orientation. However, the error formulation does become dependent on the on-path starting point.

In the current framework, the PCV path is constrained to be on a plane. To make the framework applicable for compliant (shell) mechanisms that have 3 dimensional PCV movement, the addition of an error term related to the out-of-plane rotation should be researched. So that 3D path shape can be controlled.

The presented surrogate-based solution method could be called a one layer neural network. One can improve calculation time more by utilizing a full-scale neural network. The presented framework can generate training data for the Boundary Learning Optimization Tool presented by Hatamizadeh [19]. Such a tool can generate optimized detailed designs or new insights for conceptual designs.

6 Conclusion

This paper introduced a framework to optimize the large deformation kinematic behavior of a compliant shell mechanism and applied the framework to a design example. It uses unified stiffness characterization to analyze the mechanism, and part of the Fourier descriptor characterization to characterize the PCV path.

Design variables are relevant for path shape optimization if, at least one, influences the change between incremental geometric stiffness matrices.

The framework uses a simplified version of the Fourier-descriptors. It optimizes the error between shape describing step-functions. These functions follow from normalized path segment length and orientation change between segments. Therefore, PCV path shape can be addressed independently.

Finally, this paper applied the framework to a scoliosis brace design case, to give an indication of the use and outcome of the framework. After optimization, a maximum path deviation of 0.44 $[mm]$, initial PCV location error of 0.30 $[mm]$, and a difference in orientation of 0.76 $[deg]$ remained for a POI rotation of 40.5 $[deg]$.

Acknowledgements

The writers would like to acknowledge NSF No. IIS-1527133 as well as NWO-TTW (HTSM-2012 12814: ShellMech) for the financial support of this project.

References

[1] Leemans, J., Kim, C., van de Sande, W., and Herder, J., 2018. "Unified stiffness characterization of non-linear compliant shell mechanisms". *J. Mechanisms Robotics.*

[2] van de Sande, W. W. P. J., and Herder, J. L., 2018. "Analysis of parasitic motion in compliant mechanisms using eigenwrenches and eigentwists". In Volume 5A: 42nd Mechanisms and Robotics Conference, ASME.

[3] Radaelli, G., and Herder, J., 2017. "Gravity balanced compliant shell mechanisms". *International Journal of Solids and Structures,* **118-119**, jul, pp. 78–88.

[4] Howell, L. L., 2013. *Handbook of Compliant Mechanisms*. John Wiley & Sons.

[5] Seffen, K. A., 2012. "Compliant shell mechanisms". *Philosophical Transactions of the Royal Society A: Mathematical, Physical and Engineering Sciences,* **370**(1965), mar, pp. 2010–2026.

[6] Nijssen, J. P. A., Radaelli, G., Herder, J. L., Kim, C. J., and Ring, J. B., 2017. "Design and analysis of a shell mechanism based two-fold force controlled scoliosis brace". In Volume 5A: 41st Mechanisms and Robotics Conference, ASME.

[7] Ullah, I., and Kota, S., 1997. "Optimal synthesis of mechanisms for path generation using fourier descriptors and global search methods". *Journal of Mechanical Design,* **119**(4), p. 504.

[8] Rai, A. K., Saxena, A., and Mankame, N. D., 2009. "Unified synthesis of compact planar path-generating linkages with rigid and deformable members". *Structural and Multidisciplinary Optimization,* **41**(6), dec, pp. 863–879.

[9] Mankame, N. D., and Ananthasuresh, G. K., 2007. "Synthesis of contact-aided compliant mechanisms for non-smooth path generation". *International Journal for Numerical Methods in Engineering,* **69**(12), pp. 2564–2605.

[10] Zahn, Charles T. Roskies, R. Z., 1972. "Fourier descriptors for plane closed closed curves". *IEEE Transactions on computers*.

[11] Lipkin, H Patterson, T., 1992. "Geometrical properties of modelled robot elasticity: Part i - decomposition". *DE-Vol. 45, Robotics, Spatial Mechanisms, and Mechanical Systems ASME 1992*.

[12] Forrester, A. I., and Keane, A. J., 2009. "Recent advances in surrogate-based optimization". *Progress in Aerospace Sciences,* **45**(1-3), jan, pp. 50–79.

[13] Koziel, S., Ciaurri, D. E., and Leifsson, L., 2011. "Surrogate-based methods". In *Computational Optimization, Methods and Algorithms*. Springer Berlin Heidelberg, pp. 33–59.

[14] Gutmann, H.-M., 2001. "A radial basis function method for global optimization". *Journal of Global Optimization,* **19**(3), pp. 201–227.

[15] Nijssen, J., 2017. "A type synthesis approach to compliant shell mechanisms". Master's thesis, TU Delft.

[16] MathWorks, 2018. *Global Optimization Toolbox User's Guide*. The MathWorks, Inc.

[17] Rolton, D., Nnadi, C., and Fairbank, J., 2014. "Scoliosis: a review". *Paediatrics and Child Health,* **24**(5), may, pp. 197–203.

[18] Dries, T., 2018. "A biomechanical characterization of spinal motion data for the design of a compliant scoliosis brace". Master's thesis, TU Delft.

[19] Hatamizadeh, A., Song, Y., and Hopkins, J. B., 2018. "Optimizing the geometry of flexure system topologies using the boundary learning optimization tool". *Mathematical Problems in Engineering,* **2018**, pp. 1–14.

5

Discussion & Recommendations

This chapter first discusses the contributions of this thesis and puts these contributions in perspective of the scoliosis brace. Furthermore, it recommends future research scope and scoliosis brace design work.

5.1. Discussion

The first paper introduced a 1 degree of freedom shell mechanism that circumscribes an object. The use of a shell mechanism makes it aesthetically appealing and provides geometric parameters for PCV path optimization. The mechanism has 1 DOF, as shown with finite element modeling and the experiment in chapter 3.

The conceptual mechanism meets design requirements on the isolated segment. Especially because the experiment shows that translation in the lateral direction, the first critical correction direction, is around 100 times less compliant than sagittal bending. Thus, it can provide sagittal bending mobility in a scoliosis brace. The geometric parameters allow for successive compliance vector path optimization to align the mechanism and spinal rotation axis over a large range of motion.

The first paper also showed that curvature cannot move the bending compliance vector of a non-helical shell mechanism to the object side of the pilot points. Furthermore, the bending compliance vector can be located out of mechanism material. With that, we showed an advantage of shell mechanisms and one of their limitations. These limitations lead to selecting a helix-type building block for the scoliosis brace mechanism. After selecting a building block, intelligent and intuitive design choices modified the sinusoidal-helix to be 1 DOF. These choices were supported by rigid-body kinematics and Kim's design rules [21]. They can assist with future synthesis, but they are not conclusive.

Large deformation PCV path requirements are easily formulated as the objective for the presented framework, paper 2. That framework can function as a successive design step to mechanism synthesis. It refines conceptual mechanism shape to meet large deformation design requirements, by optimizing the path of the PCV. The framework independently optimizes path shape, location, orientation, and length.

The optimized scoliosis brace mechanism closely approximates the PCV path requirements by Dries [9]. Initial PCV location is off by $0.30\ [mm]$, maximum path deviation is $0.44\ [mm]$, and the difference in orientation is $0.76\ [deg]$ over a sagittal bending range of $40.5\ [deg]$. This approaches the activities of daily living requirement, which requires 50 degrees of sagittal bending [12]. Small deviations in the PCV path can be compensated by the spine, it can engage different vertebrae to a different extent and alter the path of the sagittal bending axis.

That paper also discusses guidelines for selecting proper design variables. A set of variables can be used for PCV path shape optimization if at least one of the variables affects the change between incremental geometric stiffness-matrices. So that it affects PCV path shape.

The framework could assist with future designs of exoskeletons, braces, or rehabilitation devices because all these devices need to address the location of a rotation axis. Furthermore, it could provide interesting observations on the effect of geometric parameters in terms of mechanism behavior.

5.2. Recommendations

Mechanism design in paper 1 followed from a restriction on the shell mechanism building block library and intuitive concatenation rules. To extract the potential of the library, a synthesis method could be developed. Such a method could address building block parameterization and concatenation. It could explain the effects on the location and direction of the resulting compliance vectors and their unified compliance magnitude. The mechanism design paper in this thesis can function as a starting point to generate a synthesis method. Kim's work covers adding eigen-twists and eigen-wrenches in series and parallel [21].

The optimization search was performed with a surrogate based solution method. Using a full-scale neural network as a solution method could improve solution time significantly. Hatamizadeh developed a successive optimization tool for the FACT method called the Boundary Learning Optimization Tool [22]. That tool uses a neural network to indicate the Pareto front. Such a network could also reveal new insights in shell mechanism topology synthesis.

Furthermore, the optimization paper focuses on matching the desired PCV path and relevant design variables. Future objectives could address the robustness of a solution and design variable sensitivity is not discussed. For braces, exoskeletons, or rehabilitation devices sensitivity should be low, making the designed mechanism more robust and less sensitive to manufacturing errors or alignment with the torso.

In the current design, geometry enforces large deformation behavior. The scoliosis brace could become slimmer and more aesthetically appealing when adding material properties to the set of design variables. Stacy presented a strategy to tailor stiffnesses of composite compliant shell mechanisms utilizing thermal prestress [23].

Figure 5.1 shows a design iteration of the scoliosis brace where the isolated segment is replaced with the presented conceptual mechanism. BraceSim analyzed this brace [24]. Premature results indicate that the correction capability of this brace is limited by the fixation of the top and bottom part to the torso. The mechanism allows for mobility but does not offer support for locating the top and bottom part on the torso. The redesigned parts should account for the additional functional requirements of those parts, namely keeping themselves in place.

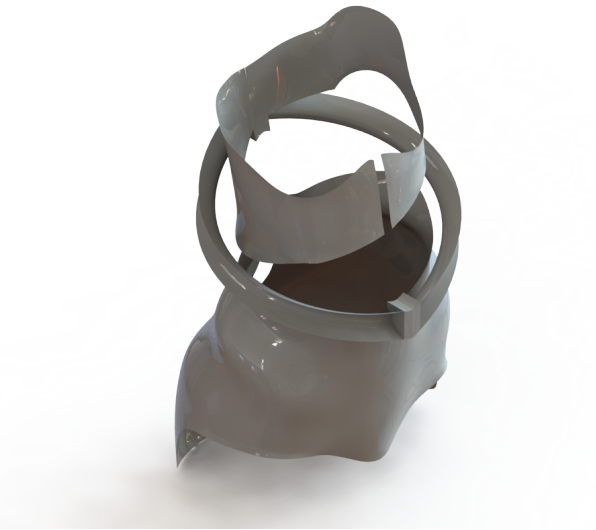

Figure 5.1: Visualization of the analyzed conceptual brace.

6

Conclusions

This thesis introduced a 1 degree of freedom shell mechanism that circumscribes an object. That mechanism is aesthetically appealing and has many geometric parameters for optimization. The freedom directions are confirmed with the unified stiffness characterization and an experiment. The generated mechanism is designed to replace the isolated segment in the scoliosis brace.

We showed that the location of the twist PCV of shell mechanism building blocks is limited to the mechanism side of the attachment points. The sinusoidal-helix shell was selected from the remaining building blocks, and mobility has been decreased according to intuitive concatenation rules. Decreasing the number of revolutions removed 2 mobility directions. Parallel concatenation of reflective symmetric shapes resulted in a 1 DOF mechanism.

The degrees of freedom of the conceptual design were experimentally validated. The experiment showed that it is around 20 times easier to perform sagittal bending than any other movement. The first critical scoliosis brace constraint directions, translation in lateral direction, is around 100 times less compliant than sagittal bending. These ratios are for the un-deformed mechanism, which is the position in which it has to correct.

Furthermore, this thesis introduced a framework to optimize the large deformation kinematic behavior of a compliant shell mechanism and applied it to the scoliosis brace design case. The can framework functions as a successive design step, it refines conceptual mechanism shape to meet large deformation design requirements. It uses unified stiffness characterization to analyze the mechanism, and part of the Fourier descriptor characterization to describe the PCV path.

The framework uses a simplified version of the Fourier descriptors. It optimizes the error between shape describing step-functions. These functions follow from normalized path segment length and orientation change between segments. Therefore, PCV path shape can be addressed independently.

Design variables are relevant for path shape optimization if, at least one, influences the change between incremental geometric stiffness matrices.

After optimization the scoliosis brace PCV path has a maximum path deviation of $0.44\ [mm]$, initial PCV location error of $0.30\ [mm]$, and a difference in orientation of $0.76\ [deg]$, compared to the path of the sagittal bending axis of the human spine over a 40.5 degrees of bending. This approaches the activities of daily living requirements, which requires 50 degrees of sagittal bending. Small deviations in the PCV path can be compensated by the spine, it can engage different vertebrae to a different extent and alter the path of the sagittal bending axis..

Finally, this thesis provided a conceptual design and optimization framework to create a mechanism for the scoliosis brace. This mechanism provides mobility for sagittal bending while transmits corrective loads. The sagittal bending axis is aligned with the PCV, preventing uncomfortable loads to the torso. The introduced mobility increases patient compliance, thus increases scoliosis bracing treatment success.

A

PCV Path-Shape Optimization Framework

Paper: Shape Optimization Framework for the Path of the Primary Compliance Vector in Compliant Mechanisms

This paper is accepted by the ASME 2019 International Design Engineering Technical Conferences & Computers and Information in Engineering Conference IDETC/CIE 2019. The paper is nearly similar to chapter 4. It limits to optimization of the shape of the path, focuses on compliant mechanisms, and the design example is more simple.

Proceedings of the ASME 2019 International Design Engineering Technical Conferences & Computers and Information in Engineering Conference
IDETC/CIE 2019
August 18-21, 2019, Anaheim, USA

DETC2019-97450

DRAFT: SHAPE OPTIMIZATION FRAMEWORK FOR THE PATH OF THE PRIMARY COMPLIANCE VECTOR IN COMPLIANT MECHANISMS

Hylke Kooistra
Dept. of Precision and Microsystems Engineering
Delft University of Technology
Delft, Zuid-Holland 2628CD
The Netherlands
Email: h.kooistra@tudelft.nl

Charles J. Kim
Dept. of Mechanical Engineering
Bucknell University
Lewisburg, Pennsylvania 17837
Email: cjk019@bucknell.edu

Werner W.P.J. van de Sande
Dept. of Precision and Microsystems Engineering
Delft University of Technology
Delft, Zuid-Holland 2628CD
The Netherlands
Email: w.w.p.j.vandeSande@tudelft.nl

Just L. Herder
Dept. of Precision and Microsystems Engineering
Delft University of Technology
Delft, Zuid-Holland 2628CD
The Netherlands
Email: j.l.Herder@tudelft.nl

ABSTRACT

The primary compliance vector captures the predominant kinematic degree of freedom of a mechanism. Its displacement describes large deformation mechanism behavior and can be an optimization objective in detailed compliant mechanism design. This paper presents a general framework for the optimization of the PCV path of compliant mechanisms using unified stiffness characterization, Fourier descriptors, and surrogate-based optimization. We found a meaningful objective formulation for the PCV path shape that is independent of path location, orientation, and length. Furthermore, we found that design variables should effect mechanism shape. Lastly, we apply the framework to an design example.

1 INTRODUCTION

The primary compliance vector (PCV) represents the predominant kinematic degree of freedom axis of a mechanism [1]. It is a generalized 6 by 1 vector representing a screw. From this vector follows the direction and location of a degree of freedom (DOF) axis. This location changes as the mechanism deforms. All locations combined form a path that characterizes large deformation behavior. Consider a cross-pivot-flexure, its PCV is in the direction of flexure width and initially located at half the height. Under large deformation it moves in the direction of the actuation, that movement is comparable to axis drift [2].

Approaches for compliant mechanism design are Pseudo-Rigid Body-model [3], structural optimization [4], or building block methods [5, 6]. Optimization does consider large deformation, but leaves little room for designer influence. Pseudo-Rigid Body-model and building block methods do not have this drawback, but focus only on the initial un-deformed topology. In this work, we present an optimization framework that refines mechanism shape to satisfy large deformation kinematic requirements. It meets these requirements by tracking the PCV path. Furthermore, we explore relevant design variables.

Ullah developed a synthesis method for end-effector path generation using Fourier descriptors [7]. These descriptors characterize a path shape independent of length, orientation, and

location. Rai and Mankame adapted this synthesis to make it suitable for end-effector path generation of hybrid planar path generators and compliant non-smooth path generators, respectively [8, 9]. However, there is limiting work on tracking the PCV of compliant mechanisms over a large range of motion.

We utilize part of Ullah, Rai, and Mankame's work for PCV path optimization of compliant mechanisms. Designing for PCV path is a more integral design approach, because one decomposition reveals force-displacement behavior and rotation-displacement relations. It is particularly useful when designing exoskeletons, braces, or rehabilitation devices.

This paper first discusses the foundation of the shape optimization framework, like mechanism characterization, path optimization and solution methods. Second, we present the framework in terms of objective function, design variables, and solution method. Third, we demonstrate the framework with an design example. Finally, we discuss the contributions of this paper and draw a conclusion.

2 BACKGROUND

Mechanism optimization involves characterization, error calculation and adapting design variables. This section discusses existing knowledge in literature on all steps of this loop. First, we elaborate on obtaining the PCV path using the unified stiffness characterization [1], this is a powerful method in analyzing the non-linear behavior of compliant mechanisms. Second, we explain the use of Fourier descriptors for path characterization [10]. Third, we discuss surrogate-based optimization.

2.1 Primary Compliance Vector

The PCV is called a eigen-twist if the predominant DOF is a rotation, for a translation it's called a eigen-wrench. The three eigen-wrenches and eigen-twists, and their corresponding stationary multiplier values of the stiffnesses or compliance, follow from Lipkin's eigen-decomposition [11].

$$K_t = \begin{bmatrix}\hat{\mathbf{w}}_f & \hat{\mathbf{w}}_\gamma\end{bmatrix} \begin{bmatrix}k_f & 0\\ 0 & k_\gamma\end{bmatrix} \begin{bmatrix}\hat{\mathbf{w}}_f\\ \hat{\mathbf{w}}_\gamma\end{bmatrix} \tag{1}$$

$$C_t = \begin{bmatrix}\hat{\mathbf{T}}_f & \hat{\mathbf{T}}_\gamma\end{bmatrix} \begin{bmatrix}a_f & 0\\ 0 & a_\gamma\end{bmatrix} \begin{bmatrix}\hat{\mathbf{T}}_f\\ \hat{\mathbf{T}}_\gamma\end{bmatrix} \tag{2}$$

Where: K_t and C_t are the tangent stiffness and compliance matrix, k_{fi} and α_{fi} are the translational stiffness and compliance multipliers for $i = 1..3$ in the direction of f_i, $k_{\gamma i}$ and $\alpha_{\gamma i}$ are the rotational stiffness and compliance multipliers in the direction of γ_i. $\hat{\mathbf{w}}_{fi}$ are the eigen-wrenches and $\hat{\mathbf{T}}_{fi}$ are the, by an eigen-wrench, induced twists. $\hat{\mathbf{T}}_{\gamma i}$ are the eigen-twists and $\hat{\mathbf{w}}_{\gamma i}$ are the, by an eigen-twist, induced wrenches.

The PCV is the eigen-twist or eigen-wrench with the largest unified compliance. Leemans' unified stiffness characterization enables a systematic and meaningful ordering of the rotational and translational compliances [1]. The unification variable χ_i expresses rotational compliance as equivalent translational compliance.

$$\tilde{\alpha}_f = \begin{bmatrix}\alpha_{f1} & \alpha_{f2} & \alpha_{f3} & \chi_1^2\alpha_{\gamma 1} & \chi_2^2\alpha_{\gamma 2} & \chi_3^2\alpha_{\gamma 3}\end{bmatrix} \tag{3}$$

$$\chi_i = \sqrt{h_i^2 + \left|\boldsymbol{r}_i\right|^2} \tag{4}$$

Where: h_i is the pitch of the eigen-twist, and $\boldsymbol{r}_i$ is the shortest vector from the point of interest (POI) on a mechanism to the line of an eigen-twist.

Incremental evaluation of the eigen-decomposition results in a PCV per time-step, because the stiffness matrix changes as the deformation increases. Together these vectors form the PCV path.

In contrast to end-effector behavior, the combination of PCV and compliance multipliers is a integral characterization approach. It covers force displacement behavior, and the relation between rotations and displacements.

2.2 Fourier Descriptors

In 1972 Zahn introduced Fourier descriptors and used them successfully for pattern recognition [10]. Ullah used these descriptors to compare the desired motion of an end-effector with the actual motion [7]. Rai and Mankame used this formulation for optimization based mechanism synthesis [8, 9].

A Fourier descriptor objective function emphasizes the similarity in shape between paths. Consider the paths in Fig. 1 and compare the blue path to the desired red path. In Fig 1a the evaluation points are at the same location for both paths, but the shape is significantly different. A structural error objective function would suggest this solution because of the smaller point to point distance. However, Fig. 1b is a better match to the desired shape. The Fourier descriptor objective function would suggest this solution, because it emphasizes shape. Furthermore, it's independent of on-path starting point, path length, orientation, and location. On-path starting point is defined as: the location of the first evaluation point relative to the path.

The objective function can express path shape independently by comparing harmonic amplitudes and phase shifts between the

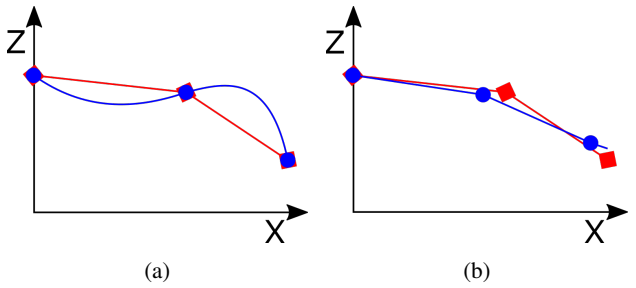

FIGURE 1: THE DESIRED SHAPE IN RED, AND THE ACTUAL SHAPE IN BLUE [9].

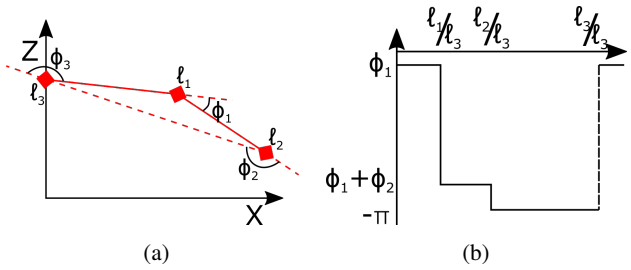

FIGURE 2: AN ARBITRARY PATH AND THE MATCHING PERIODIC STEP-FUNCTION.

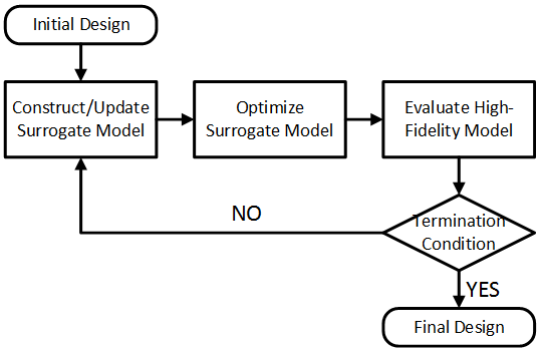

FIGURE 3: FLOWCHART OF THE SURROGATE-BASED OPTIMIZATION PROCESS.

desired and actual path. These descriptors follow from translating the path to a periodic step-function and expressing it as a Fourier-series. The amplitude of a step follows from the change in angle between line segments (ϕ). The time at which a step occurs follows from the normalized path length of a line segment ($\frac{\ell_i}{\ell_{end}}$). Connecting the first and last evaluation point to each-other closes the path and makes the step-function periodic, because the total change in angle of one loop equals $\pm 2\pi$.

In practice, parametrization of an arbitrary path with change in angle (ϕ) and arc-length (ℓ) looks like Fig. 2a. From this parametrization follows the periodic step-function in Fig. 2b. A harmonic amplitude is the magnitude of the Fourier coefficient, phase shift is the angle of this coefficient. Fourier coefficients follow from:

$$a_k = \frac{1}{T}\int_T y(t)e^{-jk\omega_0 t}dt \tag{5}$$

Where k indicates the harmonic, $x(t)$ is the step-function, and:

$$\omega_0 = \frac{2\pi}{T} \tag{6}$$

Fourier descriptors follow from angle change and arc-length. These measures are relative to the path, making the objective independent of path orientation and location. Furthermore, arc-length is scaled so that each solution has a total arc-length of 2π, thus the objective is independent of path-length.

2.3 Surrogate-Based Optimization

In surrogate-based optimization a fast and analytically tractable surrogate model replaces a computationally expensive model [12, 13]. The optimization process comprises construction, optimization, checking, and updating of the surrogate model as illustrated by Fig. 3.

Radial basis functions construct a surrogate model based on a linear combination of multiple radially symmetric functions [12, 13]. The basis functions influence nearby points more, and points far from the function center less. Combined with weight-factors for amplitudes, the sum of basis functions replicates the high-fidelity model. Figure 4 graphically constructs a surrogate model of an objective function with exponential basis functions. The blue dots are objective values of the high-fidelity model, the red line is the surrogate. Equation 7 presents the parametric relation of this model.

$$g(\mathbf{x}) = \sum_{n=1}^{N} w_n e^{-\gamma|\mathbf{x}-\mathbf{x_n}|^2} \tag{7}$$

Where: $g(\mathbf{x})$ is the surrogate model, w_n are weight-factors determining the basis function amplitude, and $\mathbf{x_n}$ determining basis function center. γ determines the influence on nearby points, N is the number of high-fidelity data points.

The main advantage of surrogate-based optimization is the decrease in calls to the objective function [13]. Which causes a large reduction of computation time for complicated objective

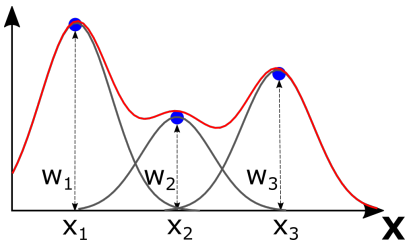

FIGURE 4: SURROGATE MODEL IN RED OF THE HIGH-FIDELITY MODEL IN BLUE, BASIS FUNCTIONS IN GRAY.

functions based on finite element modeling. Furthermore, it overcomes discontinuities, local minima, noise in the objective function, and it is easier to differentiate. Finally, an optimization with radial basis functions converges for a given search-space [14].

3 FRAMEWORK

To optimize the PCV path of a compliant mechanism, the framework should be able to deal with cumbersome FEA modeling and the designer should be able to identify key design variables. Obtaining incremental tangent stiffness matrices requires time consuming FEA, these matrices are the source of the mechanism characterization. Furthermore, only a few design variables change the path of the PCV and affect the objective as intended.

This section describes the framework that can do the above, utilizing the presented background. This section also provides guidelines in selecting design variables. We present the framework in terms of objective formulation, design variables, mapping, and solution method.

3.1 Objective Formulation

The PCV path is the path created by the series of incrementally PCV locations while deforming a mechanism, like the blue lines in Fig. 7. Path shape, location, orientation, and length characterize the PCV path over a large range of motion. Relative angle change ϕ_i and normalized arc-length ℓ_i characterize the shape. Location of the initial PCV it the best measure for path location. Orientation and length follow from the angle and distance between the initial PCV and the final PCV.

This paper focuses on the shape of the PCV path. Location and orientation are left out of the objective function, because rigid body transformations can meet these requirements. When selecting design variables that hardly influence overall compliance, path length can also be left out of the objective. Adjusting thickness or mechanism length can meet path length, after optimization.

3.1.1 Error formulation. The individual shape error calculation is scaled so that the initial design represents baseline performance. The error is scaled in such a way that error of the initial design equals unity. The conceptual design approaches the desired characteristics, thus values of unity are reasonable for the initial design. Scaling the error is useful for eventual expansion of the objective function, to include other PCV path characteristics. Scaling the individual errors of an expanded objective function makes them insightful, have a similar magnitude, and makes weight-factors solely related to the importance of a characteristic.

Equation 8 presents the total objective function. Objective expansions can be added to this equation, like path orientation, length, or location error formulations. Squaring the shape error penalizes designs that perform worse than the initial design quadratically, and award designs that perform better.

$$\begin{aligned} &\textit{minimize}: \\ &\Psi_{tot} = w_s \left(\frac{\Psi_s}{\Psi_{s_1}} \right)^2 \end{aligned} \tag{8}$$

3.1.2 Shape error. A combination of step-functions represents the shape of a PCV path. Comparing the function of the actual path to the desired path results in the error value.

The error follows from taking the absolute difference between the functions, and integrating that difference (see Eqn. 9). The integration interval equals the path length belonging to an angle change of 2π. Figure 5 is a graphical clarification of the error between the shape of the blue and red path of Fig. 6a. The left sub-figure shows both step-functions, the right sub-figure indicates error.

$$\Psi_s = \int_0^{\ell_{end}} ||y(t) - y^*(t)||dt \tag{9}$$

Section 3.2 describes the mapping of PCV locations to arc-length (ℓ) and step functions ($y(t)$). The asterisk indicates the desired path shape.

This error formulation is more simplistic than the Fourier descriptor error formulation. It consists of only one error term, and does not have to balance harmonic impact. A Fourier descriptor objective uses error in phase shift and amplitude to optimize shape, these metrics are co-dependent on the number of harmonics. Large harmonics usually have smaller amplitudes, thus the amplitudes of a high harmonic have less impact on the error compared to a low harmonic.

Like Fourier descriptors, the presented objective function is independent of path orientation, location, and length. However, it is dependent on the on-path starting point, because the representation of actual and desired shape is not periodic.

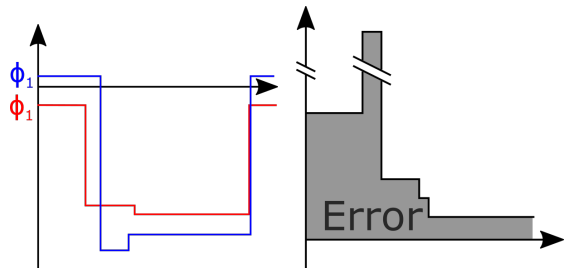

(a) (b)

FIGURE 5: THE SHAPE ERROR (IN GREY) BETWEEN THE RED AND BLUE PATH.

3.1.3 Conditions. A polygon is needed for the mapping from incremental primary compliance vectors to the shape describing step-functions. The next section discusses the actual mapping.

For the mapping to be valid, the orientation of the PCV should not change over the deformation. Furthermore, the desired and actual PCV should be aligned. The equality constraint in Eqn. 10, which is valid for a twist constraint, introduces this condition.

$$c_1 = \boldsymbol{\rho}(\mathbf{x})_i \cdot \boldsymbol{\rho}^* - 1 = 0 \tag{10}$$

Where: c_1 is the first equality constraint, and $\boldsymbol{\rho}$ is the PCV direction vector. The, hand-picked, desired PCV direction ($\boldsymbol{\rho}^*$) should not change over the deformation.

3.2 Mapping

The amplitude and location of the steps in the shape describing step-function originate in the incremental stiffness matrices. Leemans' unified stiffness characterization extracts the PCV from these matrices. This section describes how to express PCV path shape as a combination of step-functions (see Eqn. 15). The mapping starts with obtaining the PCV location vector for each load-step. Equation 11 calculates the shortest vector between the POI and a twist PCV.

$$\mathbf{r} = \frac{(\boldsymbol{\delta} - h\boldsymbol{\rho}) \times \boldsymbol{\rho}}{\boldsymbol{\rho} \bullet \boldsymbol{\rho}} \tag{11}$$

Where: $\boldsymbol{\delta}$ is the moment vector of a PCV, $\boldsymbol{\rho}$ is the direction vector, and h is the pitch:

$$h = \frac{\boldsymbol{\rho} \bullet \boldsymbol{\delta}}{\boldsymbol{\rho} \bullet \boldsymbol{\rho}} \tag{12}$$

TABLE 1: POLYGON DATA BELONGING TO AN ARBITRARY PCV PATH.

load-step	1	2	...	end
X	r_{x_1}	$\Delta x_2 + r_{x_2}$	...	$\Delta x_{end} + r_{x_{end}}$
Z	r_{z_1}	$\Delta z_2 + r_{z_2}$	...	$\Delta z_{end} + r_{z_{end}}$

Together all PCV locations form the PCV path. This path is projected on a plane and expressed as a polygon like Tab. 1. In the table, X_i is the PCV location x-component of the i^{th} load-step, and Z_i the z-component. A similar table describes the desired path, only the values are hand-picked.

From this polygon follows the length of the line segments (ℓ_i) and the change in angle between line segments ϕ_i.

$$\ell_i = \ell_{i-1} + \ell_i = \ell_{i-1} + \sqrt{(X_i - X_{i-1})^2 + (Z_i - Z_{i-1})^2} \tag{13}$$

Where: X and Z follow from Tab. 1.

$$\phi_i = \theta_i - \theta_{i-1} = \tan^{-1}\frac{(Z_i - Z_{i-1})}{(X_i - X_{i-1})} - \tan^{-1}\frac{(Z_{i-1} - Z_{i-2})}{(X_{i-1} - X_{i-2})} \tag{14}$$

Where: θ_i is the angle between a line segment i and the positive x-axis.

Lastly, arc-length and change in orientation form the step-function that describes PCV path shape:

$$y(t) = \phi_1 + \sum_{i=2}^{n} \Delta\phi_i u(t - \tilde{\ell}_{i-1}) + (\phi_1 - \phi_{end})u(t - \tilde{\ell}_{end}) \tag{15}$$

Where $u(t)$ indicates a step function, $\tilde{\ell}$ is the normalized arc-length with a periodic interval of one:

$$\tilde{\ell} = \frac{\ell}{L} \tag{16}$$

And:

$$\Delta\phi = \phi_i - \phi_{i-1} \tag{17}$$

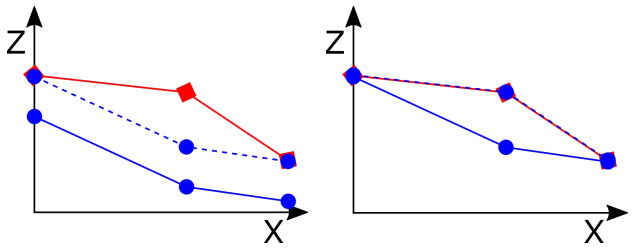

(a) LOCATION. (b) SHAPE.

FIGURE 6: THE DESIRED PATH IN RED, THE ACTUAL PATH IN BLUE, AND THE DESIGN VARIABLE EFFECT IN DASHED BLUE.

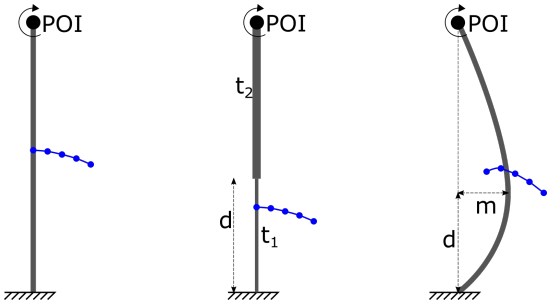

(a) (b) (c)

FIGURE 7: THREE FLEXURE GEOMETRIES WITH THEIR PCV PATH IN BLUE.

3.3 Design Variables

A set of design variables is valid if a change in their value has an effect on the value of the objective function, thus on the path of the primary compliance vector. Figure 6b is a graphical representation of the impact that a set of design variables should have on the PCV. They should change the PCV path (in blue) in such a way that it matches the desired path (in red).

The tangent compliance matrix is the inverse of the tangent stiffness matrix. This matrix can be split into two matrices, the physical stiffness matrix and the geometric stiffness matrix, see Eqn. 18 for the finite element formulation of the tangent stiffness matrix of a non-linear system [15].

$$\mathrm{C}_t^{-1} = \mathrm{K}_t = \int_V (\mathrm{B}^{\mathrm{T}}\mathrm{DB} + \mathrm{G}) dV = \mathrm{K_p} + \mathrm{K_g} \qquad (18)$$

Where: B is the differentiation matrix, D is the elasticity matrix which includes material properties, G is the geometric stiffness matrix which is equal to K_g, and K_p is the physical stiffness matrix. This last matrix (K_p) describes the initial un-deformed behavior. Whereas the geometric matrix is based on changing geometry and describes the non-linear behavior.

Because the compliance matrix contains all instantaneous kinematic characteristics of a compliant mechanism, design variables should influence the physical compliance matrix to have an effect on the initial location of the PCV (Fig. 6a). Variables to achieve this are difference in thickness or a difference in material properties.

Effecting the path of the PCV (Fig. 6b) is more challenging. If the change between incremental geometric compliance matrices differs when changing the values of the design variables, they have an impact on the trajectory of the PCV.

Geometric phenomena that cause path change are: Change in second moment of area and change in mechanism length, defined as the shortest distance between the point of interest and the point of constraint [1]. Design variables that effect these phenomena are curvature or number of corrugations.

Figure 7 shows three flexure geometries and their, from couple moment at the POI, resulting PCV path (in blue). In Fig. 7b difference in thickness along flexure length alters the initial geometry, t_1 and t_2 indicate thickness difference, d indicates the transition point between t_1 and t_2. These design variables change the initial location of the PCV. Path shape remains similar but could be scaled, because of overall compliance and relative mechanism length. The path shape of Fig. 7a can be reconstructed for any d if thicknesses are picked cleverly. These design variables chiefly effect the physical stiffness matrix.

In Fig. 7c curvature along flexure length alters the initial geometry, m indicates curvature amplitude and d indicates the vertical location of m. These design variables change the PCV path shape compared to Fig. 7a, without having a significant impact on overall compliance. These design variables effect the difference between incremental geometric stiffness matrices.

3.4 Solution Method

The selected solution method is the surrogate-based optimization algorithm in the Matlab Global Optimization Toolbox [16]. It's selected because of the earlier mentioned advantages.

An additional advantage is the requirement of lower and upper bounds on the design variables. These bounds help enforcing a search space for which the finite element model converges.

A penalty objective function implements constraints, because the surrogate-based optimization algorithm does not accept constraint equations, and because the number of FEM evaluations should be kept to a minimum. If/else statements indicate constraint violations and, if a constraint is violated, set the objective to a large value.

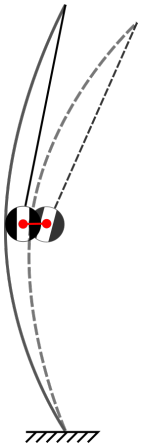

FIGURE 8: DESIRED ROD BEHAVIOR SUPPORTED BY A CURVED FLEXURE AND A RIGID ELEMENT.

4 DESIGN EXAMPLE

The design example in this section gives an indication of the use and outcome of the presented framework. First, we introduce an arbitrary design case and conceptual design. Second, we formulate the objective, followed by the parametrization and modeling of the mechanism. Finally, we present the outcome.

4.1 Case

A rod needs a support while maintaining its a rotational degree of freedom, and during rotation its center has to displace horizontally, like a rod rolling on a table. Figure 8 illustrates the problem together with a conceptual solution. Dashed lines illustrate the deformed configuration.

The conceptual design connects a curved flexure mechanism (in gray) to the rod with a rigid element (in black). When the twist compliance vector of the flexure and the axle rotational axis are aligned properly, the flexure allows for the rotational degree of freedom. However, the PCV path (in red) needs fine tuning of mechanism shape to meet the horizontal displacement requirement.

4.2 Objective

The objective is a straight line movement of the PCV. That translates to the polygon in Tab. 2. Location and orientation are not in the objective, thus a linear relation between the desired x and z components (X and Z) describes the desired PCV path. Furthermore, we select design variables that hardly effect path length, making the initial and final location of the PCV arbitrary. Equation 8 presents the objective function.

TABLE 2: POLYGON DATA BELONGING TO THE DESIRED PCV PATH.

load-step	1	2	...	end
X	0	0.001	...	0.01
Z	0	0	...	0

TABLE 3: CONSTANT CURVED FLEXURE PARAMETERS

height	0.2	[m]
width	0.1	[m]
thickness	2	[mm]
E-modulus	2	[GPa]
P-ratio	0.4	[1]

4.3 Parametrization

Design variables as suggested in Fig. 7c, curvature amplitude (m) and location of the maximum amplitude (d), are used to obtain a straight line PCV path. These variables are able to effect the shape of the PCV path, and they do not influence path length in a harming way. They effect path location and orientation, rigid body transformations can overcome misalignment of location and orientation after optimizing mechanism shape.

Other parameters like dimensions, thickness and material properties are presented in Tab. 3 and kept constant.

4.4 Finite Element Modeling

ANSYS APDL performs the finite element modeling. Key-point locations, related to the design variables and calculated by Matlab, define the geometry. The key-points form an area, this area is meshed with the SHELL181 element.

Connecting all nodes that form the top and bottom edge with RIGID184 elements achieves rigidity of these respective edges. A pilot point is added to the middle of both edges, loads and displacement constraints are applied to these points. The twist PCV over a large range of motion follows from applying a torque on the top pilot point.

APDL Math incrementally extracts the global stiffness matrix and exports it to MatLab, so that the optimization algorithm can calculate the compliance vector trajectory and determine new values for the design variables.

4.5 Result

Running a surrogate-based optimization as described in Sec. 3.4, with 200 iterations and a search space as indicated by Tab. 4, produces the optimized design in Fig. 9a. This figure also

TABLE 4: SEARCH-SPACE BOUNDS

	Amplitude (m)	location (d)
lower-bound	-0.2	0.1 *height*
upper-bound	0.2	0.9 *height*

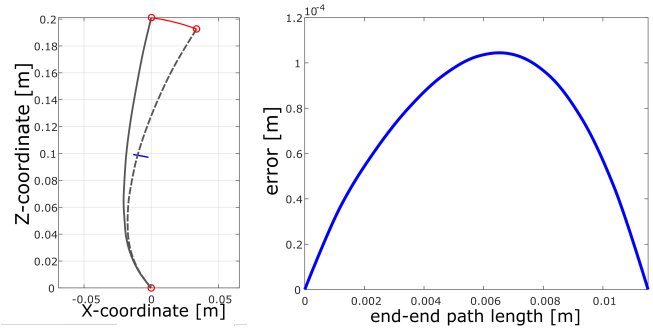

(a) (b)

FIGURE 9: RESULTING PCV TRAJECTORY OF THE OPTIMIZED CURVED FLEXURE DESIGN

gives insight in the performance of the optimized geometry. The PCV path (in blue) closely approaches the desired straight-line path shape. Figure 9b presents the the perpendicular distance between the desired horizontal path and the actual PCV path. It shows that the maximum deviation is 0.1 *mm* over a PCV path length of 12 *mm*, and a POI rotation of 19.5 $[deg]$.

5 DISCUSSION

The presented framework can tune large deformation behavior by optimizing the motion of the PCV. The framework independently optimizes path shape, because path is characterized in such a way that path length is normalized and orientation and length are excluded. The results of the design example in the previous section clearly show the capabilities of the framework. There is only a marginal error between desired and actual PCV path (see Fig. 9b).

It is easy to translate design requirements to the objective formulation, especially for exoskeletons, braces, or rehabilitations devices. All these applications need to follow the rotational degree of freedom axis of a human joint, which translates directly to the PCV path.

Design variables have a significant impact on the solution space. The set of design variables in the design example are able to achieve the objective, because they effect the change in incremental stiffness matrices. If they do not effect this change, they hardly influence the shape of PCV path. Causing a small solution space, that probably won't contain a well performing design.

Compared to compliant mechanisms, shell mechanisms have greater design flexibility to meet functional and geometrical requirements [17, 18]. Their shape is characterized by more parameters, thus their solution space is larger. In future work, the presented framework can be utilized to capitalize on larger design flexibility of shell mechanisms.

This framework uses Fourier-descriptor path characterization. However, it does not compare harmonic amplitudes and phase shifts in the objective. Comparing the, path describing, step-functions simplifies the objective. It maintains the separation between shape, location, and orientation. However, the error formulation does become dependent on the on-path starting point.

In the current framework, the PCV path is constraint to be on a plane. To make the framework applicable for compliant (shell) mechanisms that have 3 dimensional PCV movement, the addition of an error term related to the out-of-plane rotation should be researched. So that 3D path shape can be controlled.

Rigid body transformations performed by the designer are supposed to overcome errors in location or orientation. However, the available design space might prevent these transformations. Additional objective formulations and design variables, addressing these path characteristics can overcome design space restrictions.

The presented surrogate-based solution method could be called a one layer neural network. One can improve calculation time more by utilizing a full scale neural network. The presented framework can generate training data for a the Boundary Learning Optimization Tool presented by Hatamizadeh [19]. Such a tool can generate optimized detailed designs, or new insights for conceptual designs.

6 CONCLUSION

This paper introduced a framework to optimize the large deformation kinematic behavior of a compliant mechanism, and applied the framework to an design example. It uses unified stiffness characterization to analyze the mechanism, and part of the Fourier descriptor characterization to characterize the PCV path.

Design variables are relevant if, at least one, influences the change between incremental geometric stiffness matrices.

The framework uses a simplified version of the Fourier-descriptors. It optimizes the error between shape describing step-functions. These functions follow from normalized path segment length, and orientation change between segments. Therefore, PCV path shape can be addressed independently.

Finally, this paper applied the framework to an arbitrary design case, to give an indication of the use and outcome of the framework. After optimization, a maximum path deviation of 0.1 *mm* remained.

ACKNOWLEDGMENT

The writers would like to acknowledge NSF No. IIS-1527133 as well as NWO-TTW (HTSM-2012 12814: ShellMech) for the financial support of this project.

REFERENCES

[1] Leemans, J., Kim, C., van de Sande, W., and Herder, J., 2018. "Unified stiffness characterization of non-linear compliant shell mechanisms". *J. Mechanisms Robotics.*

[2] van de Sande, W. W. P. J., and Herder, J. L., 2018. "Analysis of parasitic motion in compliant mechanisms using eigenwrenches and eigentwists". In Volume 5A: 42nd Mechanisms and Robotics Conference, ASME.

[3] Howell, L. L., 2001. *Compliant Mechanisms*. Wiley.

[4] Sigmund, O., 1997. "On the design of compliant mechanisms using topology optimization". *Mechanics of Structures and Machines,* ***25***(4), jan, pp. 493–524.

[5] Krishnan, G., Kim, C., and Kota, S., 2011. "An intrinsic geometric framework for the building block synthesis of single point compliant mechanisms". *Journal of Mechanisms and Robotics,* ***3***(1), p. 011001.

[6] Hopkins, J. B., and Culpepper, M. L., 2010. "Synthesis of multi-degree of freedom, parallel flexure system concepts via freedom and constraint topology (FACT) – part i: Principles". *Precision Engineering,* ***34***(2), apr, pp. 259–270.

[7] Ullah, I., and Kota, S., 1997. "Optimal synthesis of mechanisms for path generation using fourier descriptors and global search methods". *Journal of Mechanical Design,* ***119***(4), p. 504.

[8] Rai, A. K., Saxena, A., and Mankame, N. D., 2009. "Unified synthesis of compact planar path-generating linkages with rigid and deformable members". *Structural and Multidisciplinary Optimization,* ***41***(6), dec, pp. 863–879.

[9] Mankame, N. D., and Ananthasuresh, G. K., 2007. "Synthesis of contact-aided compliant mechanisms for non-smooth path generation". *International Journal for Numerical Methods in Engineering,* ***69***(12), pp. 2564–2605.

[10] Zahn, Charles T. Roskies, R. Z., 1972. "Fourier descriptors for plane closed closed curves". *IEEE Transactions on computers*.

[11] Lipkin, H Patterson, T., 1992. "Geometrical properties of modelled robot elasticity: Part i - decomposition". *DE-Vol. 45, Robotics, Spatial Mechanisms, and Mechanical Systems ASME 1992*.

[12] Forrester, A. I., and Keane, A. J., 2009. "Recent advances in surrogate-based optimization". *Progress in Aerospace Sciences,* ***45***(1-3), jan, pp. 50–79.

[13] Koziel, S., Ciaurri, D. E., and Leifsson, L., 2011. "Surrogate-based methods". In *Computational Optimization, Methods and Algorithms*. Springer Berlin Heidelberg, pp. 33–59.

[14] Gutmann, H.-M., 2001. "A radial basis function method for global optimization". *Journal of Global Optimization,* ***19***(3), pp. 201–227.

[15] Nijssen, J., 2017. "A type synthesis approach to compliant shell mechanisms". Master's thesis, TU Delft.

[16] MathWorks, 2018. *Global Optimization Toolbox User's Guide*. The MathWorks, Inc.

[17] Radaelli, G., and Herder, J., 2017. "Gravity balanced compliant shell mechanisms". *International Journal of Solids and Structures,* ***118-119***, jul, pp. 78–88.

[18] Seffen, K. A., 2012. "Compliant shell mechanisms". *Philosophical Transactions of the Royal Society A: Mathematical, Physical and Engineering Sciences,* ***370***(1965), mar, pp. 2010–2026.

[19] Hatamizadeh, A., Song, Y., and Hopkins, J. B., 2018. "Optimizing the geometry of flexure system topologies using the boundary learning optimization tool". *Mathematical Problems in Engineering,* ***2018***, pp. 1–14.

B

Experimental Data

This appendix presents additional experimental data. It contains the loading plots from which the stiffness matrices are calculated and the force-displacement plots of the glass fiber samples.

Table B.1 one presents orientation and geometric properties of the glass fiber sample. Stiffness follows from the linear part of Fig. B.1. Equation B.1 calculates Young's modulus.

$$E = k\frac{L}{A} \tag{B.1}$$

Table B.1: glass fiber samples

Sample	Orientation	Length	Width	Thickness	Stiffness	E-Modulus
1	0 [deg]	40 [mm]	10 [mm]	1.1 [mm]	1.2 [MN/m]	4.2 [GPa]
2	0 [deg]	40 [mm]	9.4 [mm]	1.1 [mm]	0.89 [MN/m]	3.4 [GPa]
3	0 [deg]	20 [mm]	9.5 [mm]	1.1 [mm]	1.8 [MN/m]	3.4 [GPa]
4	0 [deg]	20 [mm]	9.8 [mm]	1.1 [mm]	1.8 [MN/m]	3.3 [GPa]
5	90 [deg]	20 [mm]	11 [mm]	0.90 [mm]	1.8 [MN/m]	3.7 [GPa]
6	90 [deg]	20 [mm]	11 [mm]	1.1 [mm]	1.7 [MN/m]	3.1 [GPa]

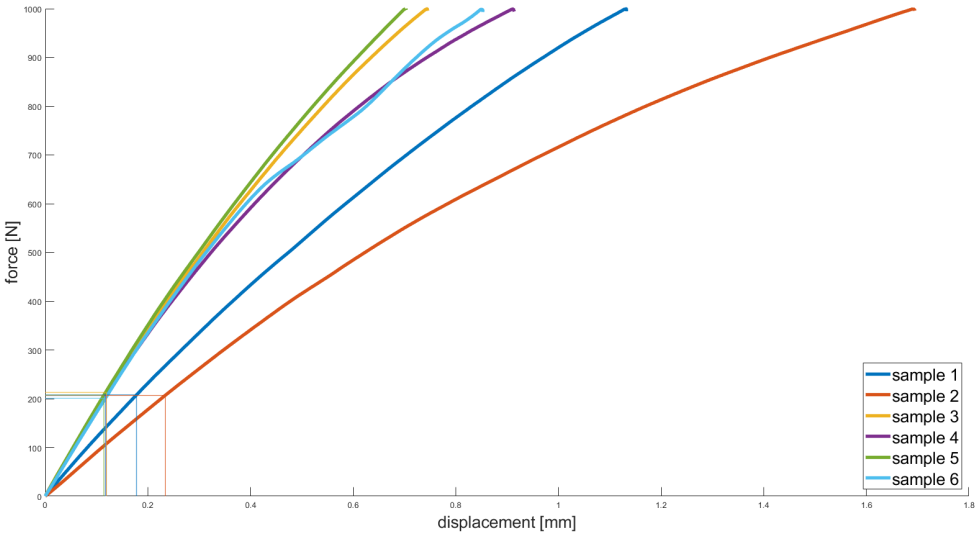

Figure B.1: Force displacement curves of multiple glass fiber samples

The loading plots present the measured load in one direction versus time samples during the experiment. Colors indicate the induced displacements. Rotation magnitude is 0.5 degrees in both directions, translation magnitude is 1.0 millimeter in both directions. These displacements are induced at 6 evaluation locations along the sagittal bending trajectory, 2, 4, 6, 8, and 10 degrees. Resulting in 3 stiffness matrices per location.

To obtain the effect of a small rotation around the y-axis, one has to read the load magnitude in the red areas of all plots. Each plot indicates the reactive load in the direction of the plot, as result of the small rotation around the y-axis.

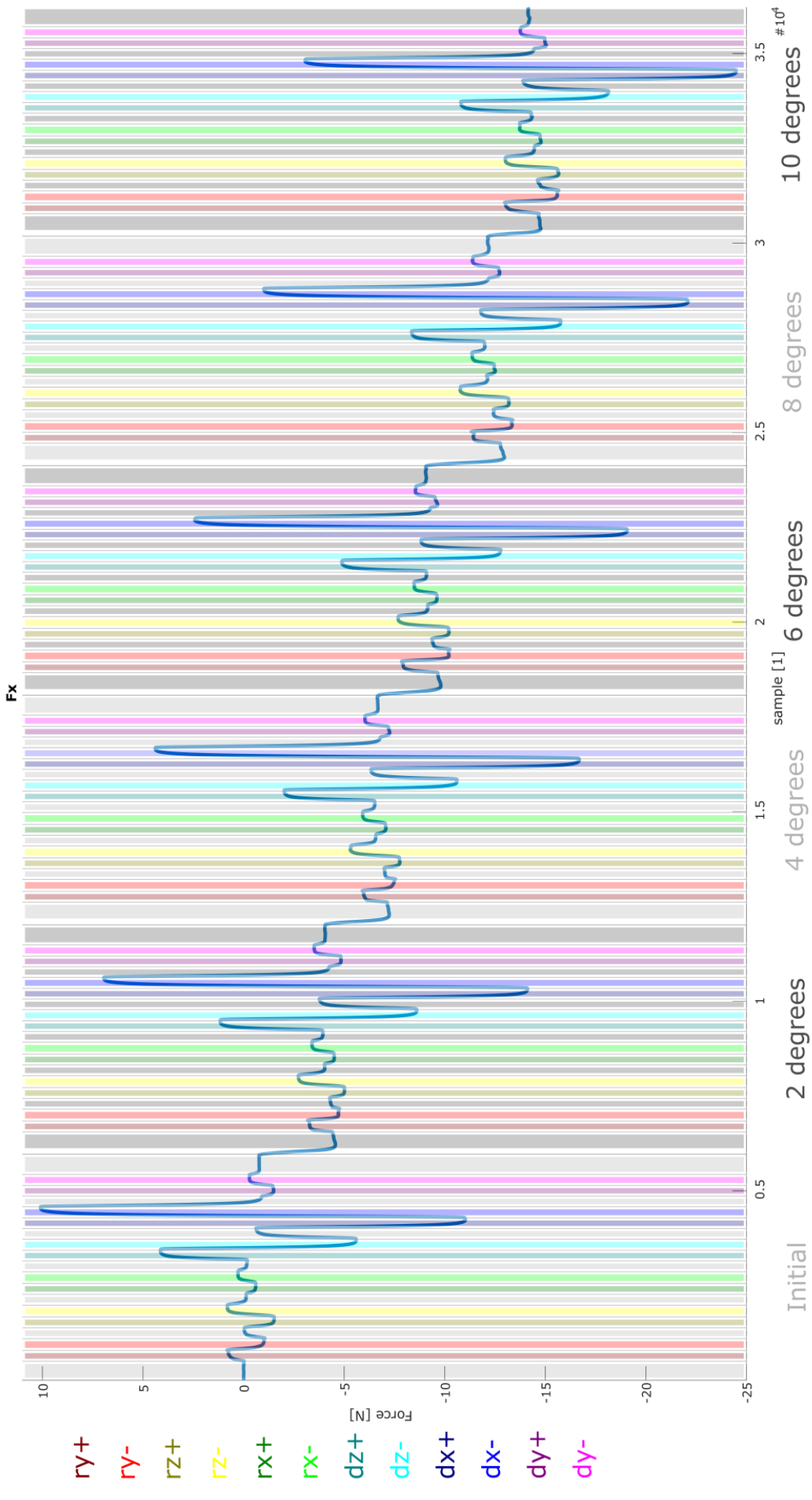
Fx
Force [N]
sample [1]
#10⁴
Initial
2 degrees
4 degrees
6 degrees
8 degrees
10 degrees
ry+
ry-
rz+
rz-
rx+
rx-
dz+
dz-
dx+
dx-
dy+
dy-

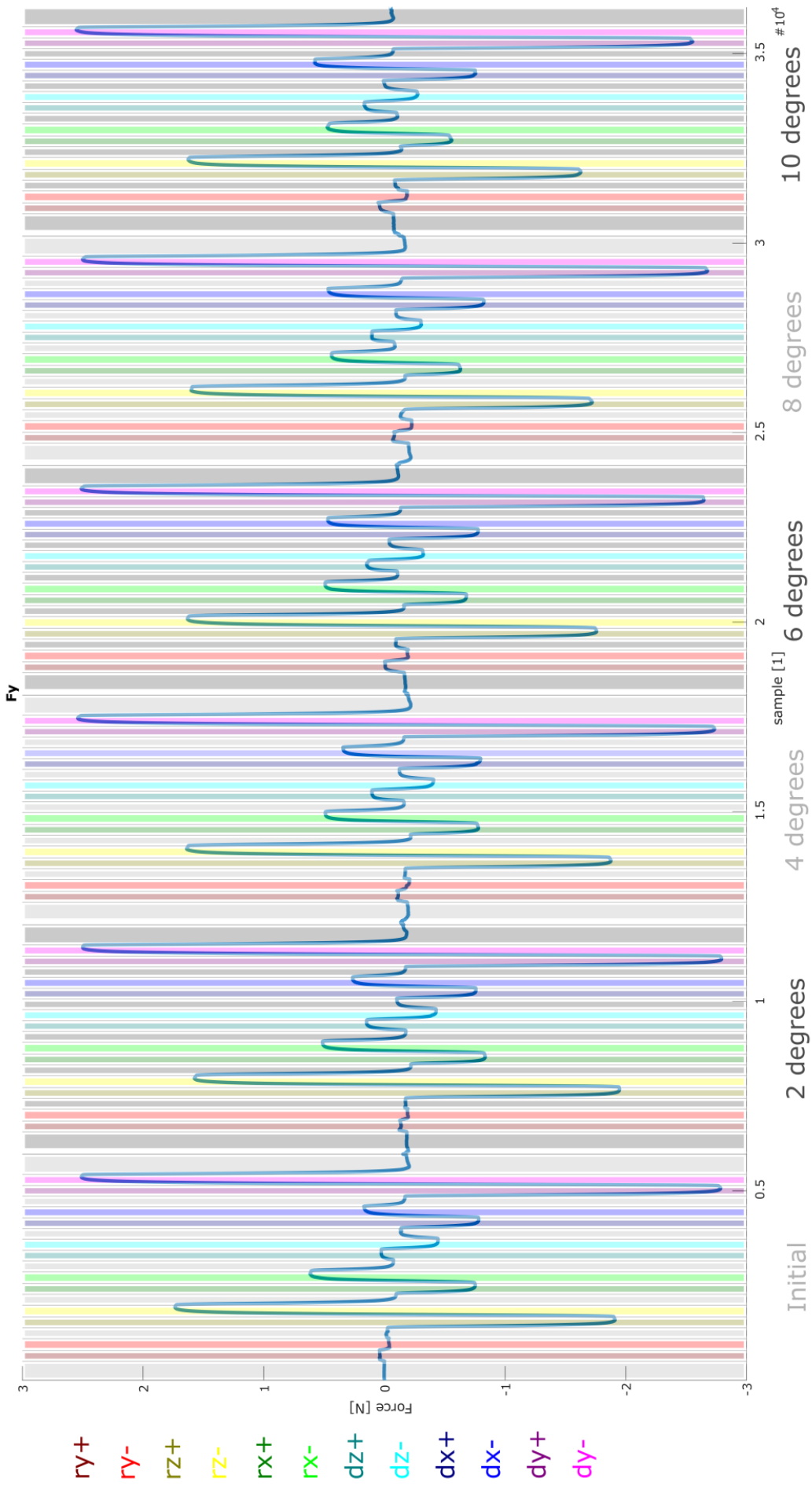
Fy
Force [N]
sample [1]
#10^4
Initial
2 degrees
4 degrees
6 degrees
8 degrees
10 degrees
ry+
ry-
rz+
rz-
rx+
rx-
dz+
dz-
dx+
dx-
dy+
dy-

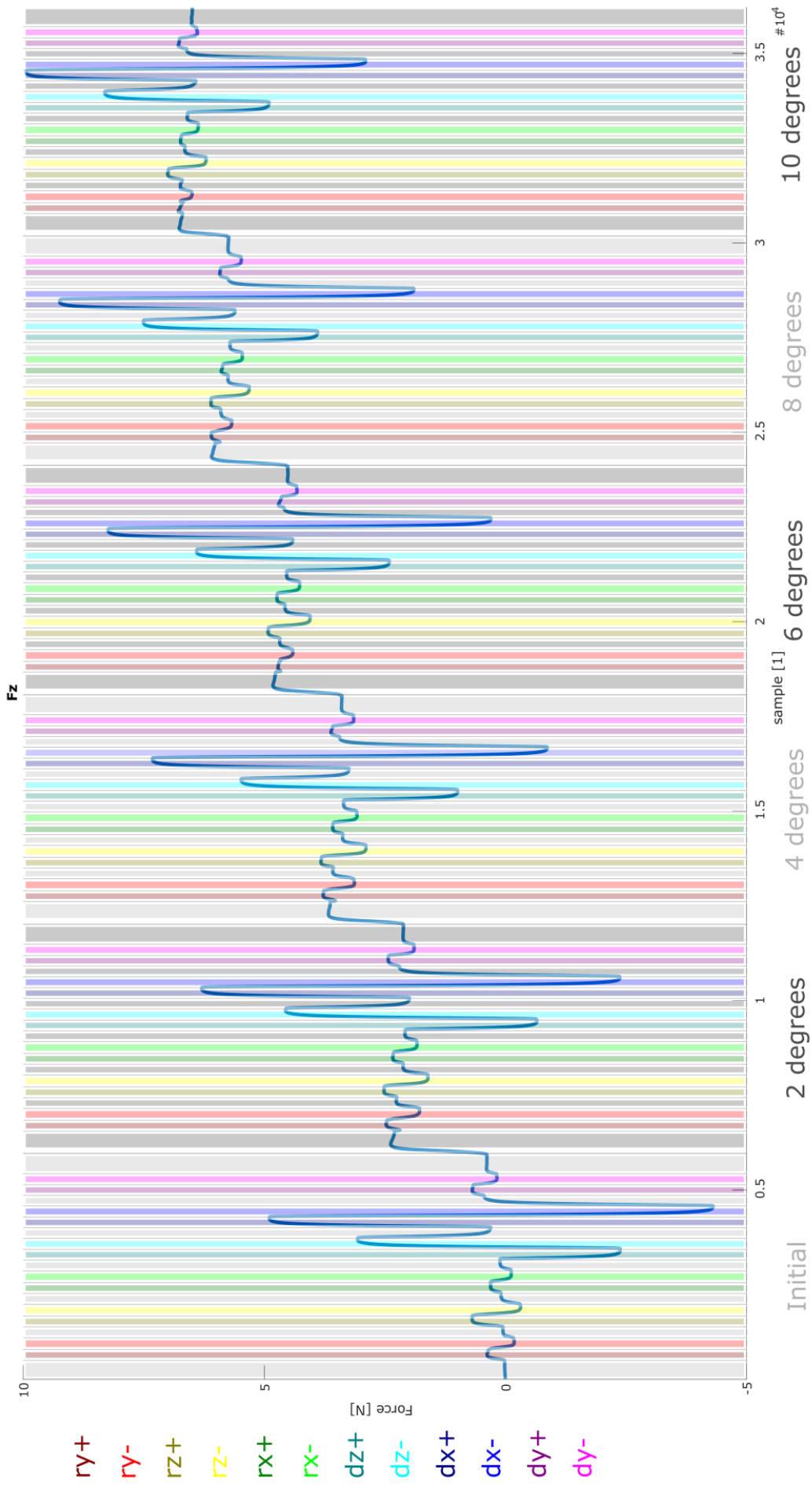
Fz
Force [N]
10
5
0
-5
sample [1]
0.5
1
1.5
2
2.5
3
3.5
#10^4
Initial
2 degrees
4 degrees
6 degrees
8 degrees
10 degrees
ry+
ry-
rz+
rz-
rx+
rx-
dz+
dz-
dx+
dx-
dy+
dy-

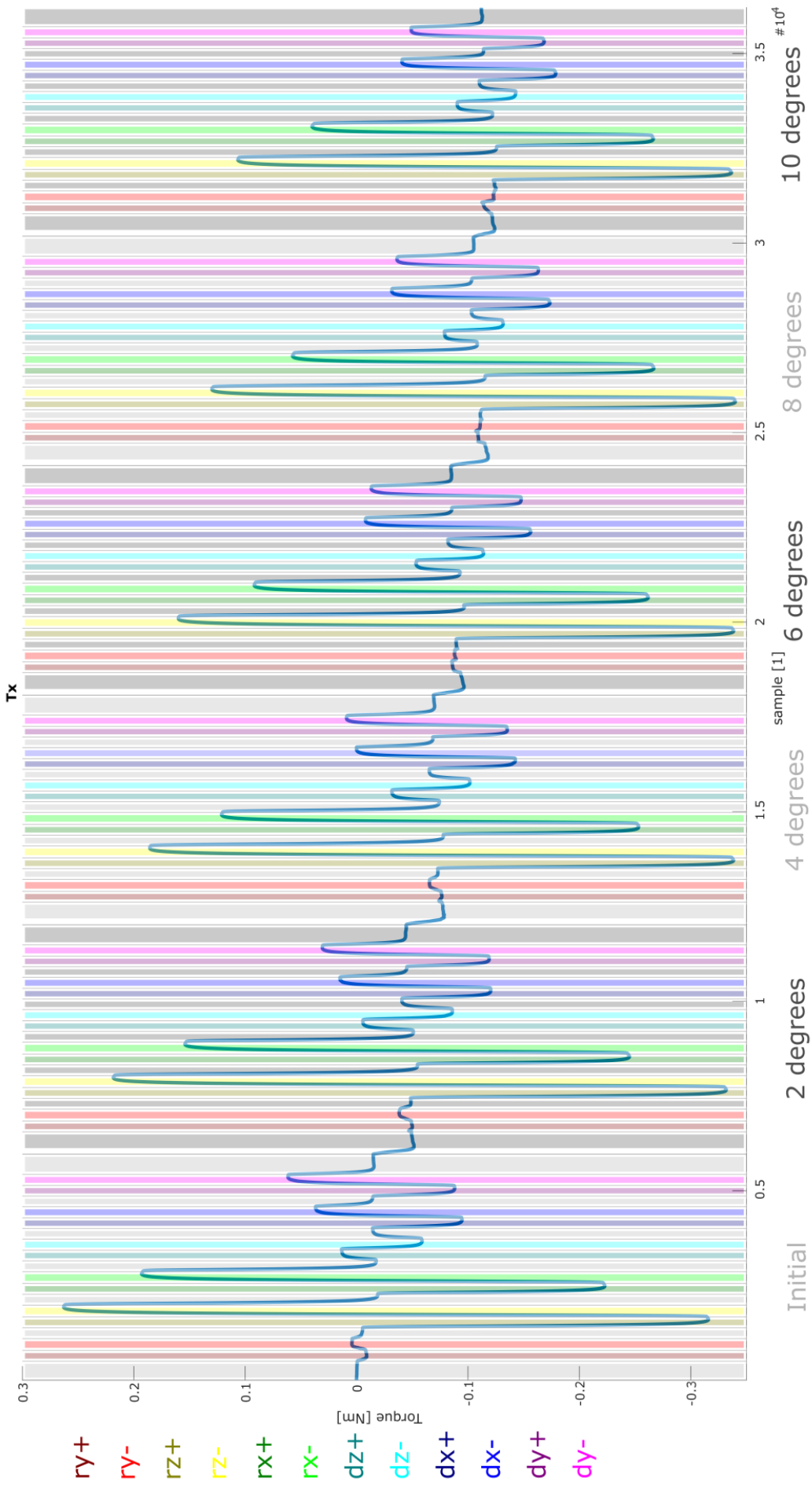
Tx
Torque [Nm]
0.3
0.2
0.1
0
-0.1
-0.2
-0.3
sample [1]
0.5
1
1.5
2
2.5
3
3.5
#10^4
Initial
2 degrees
4 degrees
6 degrees
8 degrees
10 degrees
ry+
ry-
rz+
rz-
rx+
rx-
dz+
dz-
dx+
dx-
dy+
dy-

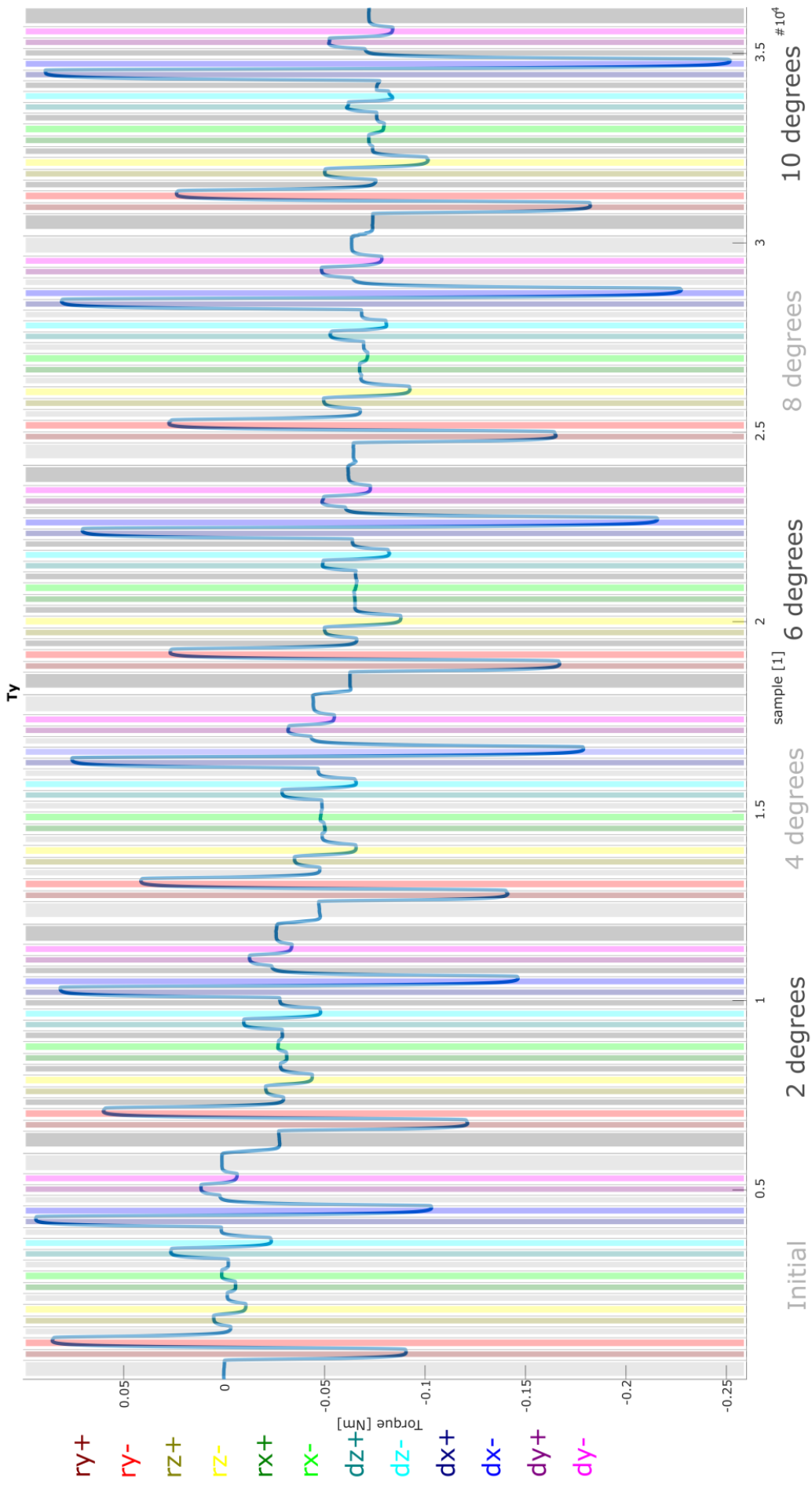
Ty
Torque [Nm]
0.05
0
-0.05
-0.1
-0.15
-0.2
-0.25
sample [1]
0.5
1
1.5
2
2.5
3
3.5
#10⁴
Initial
2 degrees
4 degrees
6 degrees
8 degrees
10 degrees
ry+
ry-
rz+
rz-
rx+
rx-
dz+
dz-
dx+
dx-
dy+
dy-

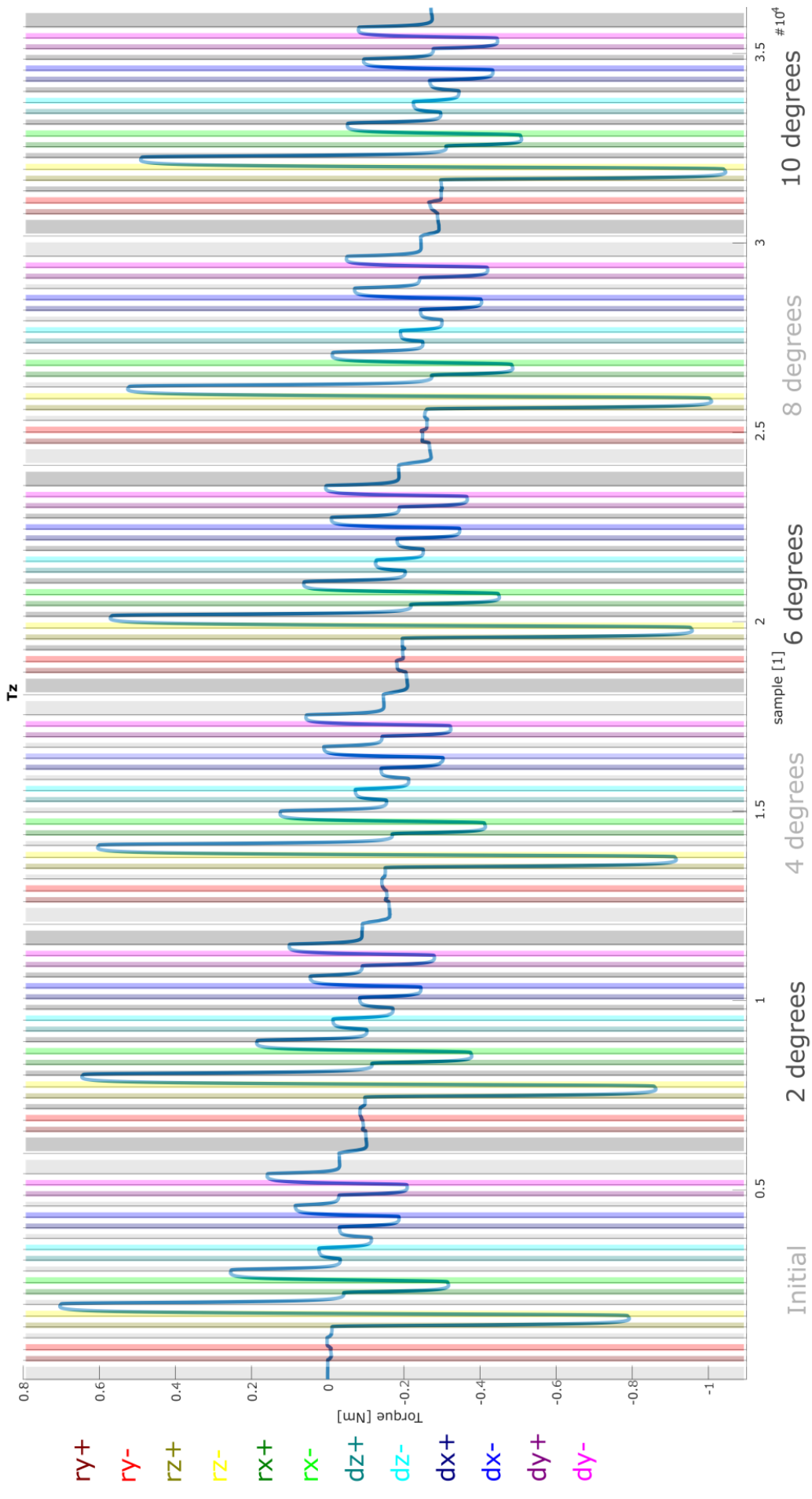
Tz
Torque [Nm]
0.8
0.6
0.4
0.2
0
-0.2
-0.4
-0.6
-0.8
-1
0.5
1
1.5
2
2.5
3
3.5
#10^4
sample [1]
Initial
2 degrees
4 degrees
6 degrees
8 degrees
10 degrees
ry+
ry-
rz+
rz-
rx+
rx-
dz+
dz-
dx+
dx-
dy+
dy-

C

Shell Mechanism Characterization with ANSYS APDL

This appendix discusses the main steps in calculating eigen-wrenches and eigen-twists of compliant shell mechanisms in MatLab, based on a finite element simulation using ANSYS. Doing the calculations in MatLab creates the opportunity to do design optimization etc. For these calculations the stiffness-matrix of the point of interest is the most relevant output of the ANSYS simulation. The steps in achieving this are discussed in multiple sections: First writing an ANSYS script, calling ANSYS from MatLab and loading ANSYS results in MatLab are described. Followed with the creation of the geometric model based on certain parameters, and meshing of this model with appropriate elements. In the fourth section boundary conditions and loading are discussed. And last the steps required for extracting the stiffness matrix are elaborated on.

MatLab – ANSYS Interaction

For the interaction between ANSYS and MatLab three file types are used: Text files are created, and a mac-file and m-files are written. ANSYS can be run in batch-mode which is started with a line of MatLab code, telling the computer to run an ANSYS simulation based on the indicated mac-file. This mac-file contains APDL code to read text files containing geometric data, loads etc. Also, the meshing, solver options, and boundary conditions are coded in this file. Some lines of code to export more results can be added.

```
SET KMP_STACKSIZE=4096K & "C:\Program Files\ANSYS ...
    Inc\v190\ansys\bin\winx64\ANSYS190.exe" -b -m 4096 -i APDL.mac -o pre.txt
```

Text files are the main channel for ANSYS and MatLab to communicate with each other, because both software can easily read and write this file type. The following command sequence is needed to write a text file with MatLab:

```
fileID = fopen('knots.txt','w');
fprintf(fileID,'%c, %i, %f, %f, %f \n','K',index,kx(i,j),ky(i,j),kz(i,j));
fclose(fileID);
```

To read the created text file with ANSYS this APDL code is needed:

```
/INPUT,'knots','txt'
```

APDL code is used extract relevant values from the simulation and assign in to a parameter. The parameter(s) are written to a text will with this command sequence in the mac-file:

```
nodenum = NODE((KX(11)+KX(15))/2,(KY(11)+KY(15))/2,(KZ(11)+KZ(15))/2)
```

```
2
3 *CFOPEN,poilocation,txt
4 *VWRITE, NX(nodenum), NY(nodenum), NZ(nodenum)
5 %f%/%f%/%f
6 *CFCLOS
```

And finally loading text-files to the MatLab workspace:

```
1 poilocation = textread('poilocation.txt','%f');
```

Geometric Modelling

Key-point locations are calculated in MatLab based on the geometric equations describing the compliant shell mechanism and written to a text-file to be read by ANSYS. Relevant key-point locations depend on how the surface area of the mechanism is created. Some possibilities are (figure C.1: patched areas, dragging a cross-section along a line, or connecting multiple cross-sections with a skin. The first option requires for key-points per patch, the second option requires key-points defining a line and key-points defining the cross-section, the last options requires key-points for multiple cross-sections. The mechanism has to be described as a surface to suit the shell elements discussed in the next section. Option two results in the smoothest area while maintaining control over the cross-section.

Because the geometric equations are described based on parameters, the geometry in ANSYS can be

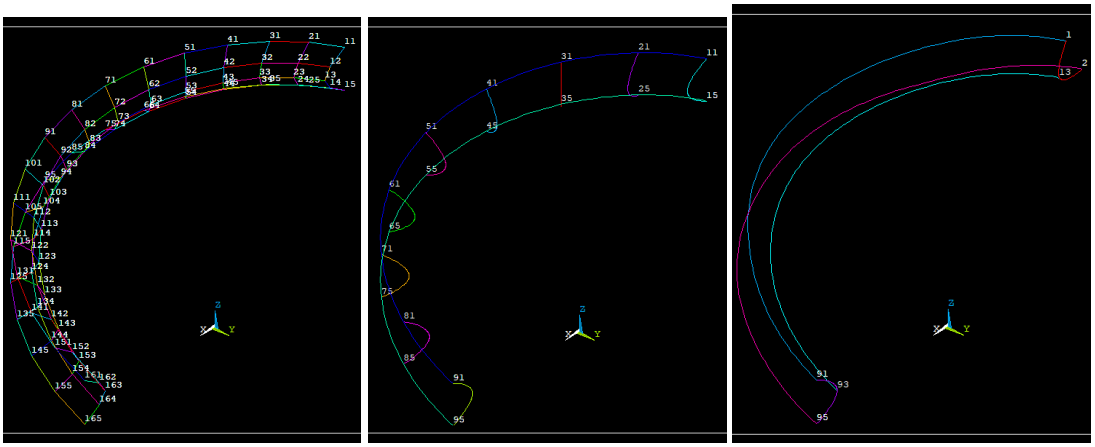

(a) Area created with many smaller areas (patches)

(b) Area created by skinning multiple cross-sections

(c) Area created by dragging a cross-section along a line

Figure C.1: Different ways of creating the mechanism's geometry in ANSYS

adjusted by changing one or multiple of those parameters in MatLab, causing the key-points to move and thus altering the surface (shape of the compliant shell mechanism).

```
1 BSPLIN, 11, 12, 13, 14, 15      ! create B-Spline based on KPs
2 BSPLIN, 21, 22, 23, 24, 25      ! create B-Spline based on KPs
3
4 ASKIN, 1, 2, 3, 4, 5, 6, 7, 8, 9! create area based on lines
```

Creating surface in APDL

Elements and Meshing

The selected element is the SHELL181 element. An analysis on multiple elements to model thin-walled structures with linear material indicates that the SHELL181 offers good answers and is the most efficient. These results are obtained with an quad mesh. To influence the location of nodes and make sure a node exists at the evaluation point, the number of elements on the edges of the surface is

controlled in the MAC file.
The keyoptions have to be set depending on the shape and loading of the mechanism. In case of the brace mechanism keyopt(5) is set to 1 to account for initial shell curvature, keyopt(3) is set to 2 so that the mesh can be on the coarse side which limits the size of the system matrix, and keyopt(1) is set to 0 to account for bending and membrane stiffness. Setting this keyopt to another value keeps the simulation from generating a stiffness matrix.

```
ET,1,SHELL181
KEYOPT,1,1,0
KEYOPT,1,3,2
KEYOPT,1,5,1

SECTYPE,1,SHELL
SECDATA,thickness,1      !set thickness
MP,EX,1,YoungsM          !set Young's modulus
MP,PRXY,1,PoissionsR     !set Poission's ratio
```

Setting element and keyopts in APDL

```
TYPE,1
MAT,1
MESHKEY,1
MESHSHAPE,0,2D
LESIZE,1,,,10,,,,,0 !number of elements on short edge
LESIZE,2,,,10,,,,,0 !number of elements on cross-section line
LESIZE,3,,,10,,,,,0 !number of elements on short edge

LESIZE,17,,,60,,,,,0!number of elements on long edge
LESIZE,18,,,60,,,,,0!number of elements on long edge
AMESH,ALL
```

Setting mesh in APDL

Loading and Boundary Conditions

The behaviour of a compliant shell mechanism is heavily depended on its boundary conditions. A fully clamped edge fixes the edge cross-section under large deformation. To obtain representative values these rigid elements have to be implemented with the boundary conditions. The actuated edge is the most challenging, because loads can only be applied to a key-point or a node, and because the stiffness matrix is evaluated at one node as well. Therefore, a way of making the actuated edge rigid has to be found so that the applied load is distributed along the entire edge and the displacement is similar along the edge.
The suggested way to do this is with the rigid 184 element and keyoption(1)=1 to have 6 rigid DOFs. These elements connect a pilot point to all the nodes on the edge of the shell and the row of nodes next to the edge. Because the modelled mechanism does not have an actual edge at the point of interest, three rows of nodes are connected to the pilot point. Loads are applied to the pilot point and the stiffness matrix is evaluated a this point as-well The get more trustworthy results the fixed point of the mechanism is constrained with a pilot point and rigid 184 elements too.

```
ET,2,184
KEYOPT,2,1,1

TYPE,2
N,,(KX(11)+KX(15))/2,(KY(11)+KY(15))/2,(KZ(11)+KZ(15))/2 !actuated pilot point
N,,(KX(91)+KX(95))/2,(KY(91)+KY(95))/2,(KZ(91)+KZ(95))/2 !fixed pilot point
E,1321,1
E,1321,132

E,1322,731
```

Setting boundaries in APDL

To evaluate the stiffness matrix incrementally for large deformation, loading is applied in time-steps After a time-step the solver pauses so that the system matrix can be stored. Also, because of different types of DOF-orderings in ANSYS (to speed up calculations) loads cannot be applied to and the stiffness matrix cannot be evaluated at redundant nodes (partly covered with the LEMESH comment in the previous section).

Extracting the Stiffness Matrix

As mentioned above the system matrix is written to a text-file after every load step with the following APDL command:

```
1 *SMAT, matk, D, IMPORT, FULL, file.full, STIFF
2 *EXPORT, matk, MMF, matkMMF1.txt
```

This sparse matrix is written in MMF format which can be loaded into MatLab with the MMREAD function. The matrix is ordered based on boundary conditions which is different from the user ordering, ordering based on increasing node number. Because the node of interest, at which the stiffness matrix is evaluated, is defined in external ordering some transformations are needed (see figure C.2). The mapping vectors are imported from the file.full and written to a text-file so that the relevant values of these vectors can be used by a MatLab script to select the indices of the system matrix matching the node of interest. Because the mechanism is not re-meshed between load steps, the mapping vectors do not change between load steps and thus evaluating them once is sufficient.

Once the indices of the node of interest in solver ordering are known the compliance matrix of the

Figure C.2: Mapping vectors between different nodal orderings.

mechanism can be assembled based on the inverse of the system matrix. The need for inverting the system matrix and assembling the compliance matrix in stead of the stiffness matrix becomes clear form the force displacement equations and the fact that the applied load is known. In case of the stiffness matrix: the components of the 6 by 6 matrix are a combination of multiple components of the system matrix. In case of the compliance matrix: the components of the 6 by 6 matrix are equal to the components, indicated by the mapping vector, of the inverse system matrix.

$$\mathrm{f} = \mathrm{K} * \mathrm{u}$$

$$\begin{bmatrix} f_1 \\ f_2 \\ \cdot \\ \cdot \\ \cdot \\ f_n \end{bmatrix} = \begin{bmatrix} K_{11} & K_{12} & \cdot & \cdot & \cdot & K_{1n} \\ K_{21} & K_{22} & \cdot & \cdot & \cdot & K_{2n} \\ \cdot & \cdot & \cdot & & & \cdot \\ \cdot & \cdot & & \cdot & & \cdot \\ \cdot & \cdot & & & \cdot & \cdot \\ K_{n1} & K_{n2} & \cdot & \cdot & \cdot & K_{nn} \end{bmatrix} \begin{bmatrix} u_1 \\ u_2 \\ \cdot \\ \cdot \\ \cdot \\ u_n \end{bmatrix} \tag{C.1}$$

$$\mathrm{u} = \mathrm{C} * \mathrm{f}$$

$$\begin{bmatrix} u_1 \\ u_2 \\ \cdot \\ \cdot \\ \cdot \\ u_n \end{bmatrix} = \begin{bmatrix} C_{11} & C_{12} & \cdot & \cdot & \cdot & C_{1n} \\ C_{21} & C_{22} & \cdot & \cdot & \cdot & C_{2n} \\ \cdot & \cdot & \cdot & & & \cdot \\ \cdot & \cdot & & \cdot & & \cdot \\ \cdot & \cdot & & & \cdot & \cdot \\ C_{n1} & C_{n2} & \cdot & \cdot & \cdot & C_{nn} \end{bmatrix} \begin{bmatrix} f_1 \\ f_2 \\ \cdot \\ \cdot \\ \cdot \\ f_n \end{bmatrix} \tag{C.2}$$

When this 6 by 6 compliance matrix is inverted again the desired stiffness matrix is extracted and the eigen-twist analyses can be performed.

```
forward = mapforward(nodenum)
*DIM,index,ARRAY,6,1,1
*DO,i,1,6
    index(i,1,1) = (forward-1)*6+i
*ENDDO
*CFOPEN,forwardv,txt
*VWRITE,index(1),index(2),index(3),index(4),index(5),index(6)
%I%/%I%/%I%/%I%/%I%/%I
*CFCLOS
```

Forward mapping vector in APDL

```
forwardv = textread('forwardv.txt','%f');
Nod2Bcs = dlmread('Nod2Bcs.txt',':',2,1);
index = Nod2Bcs(forwardv);

for i = 1:loadstep
    filename = sprintf('%s%i%s','matkMMF',i,'.txt');
    Kbcs = MMREAD(filename);
    Cbcs = inv(Kbcs);
    Cend{i} = full(Cbcs(index,index));
    Kend{i} = inv(Cend{i});
end
```

Mapping and extracting stiffness matrix MatLab

Graphical Overview

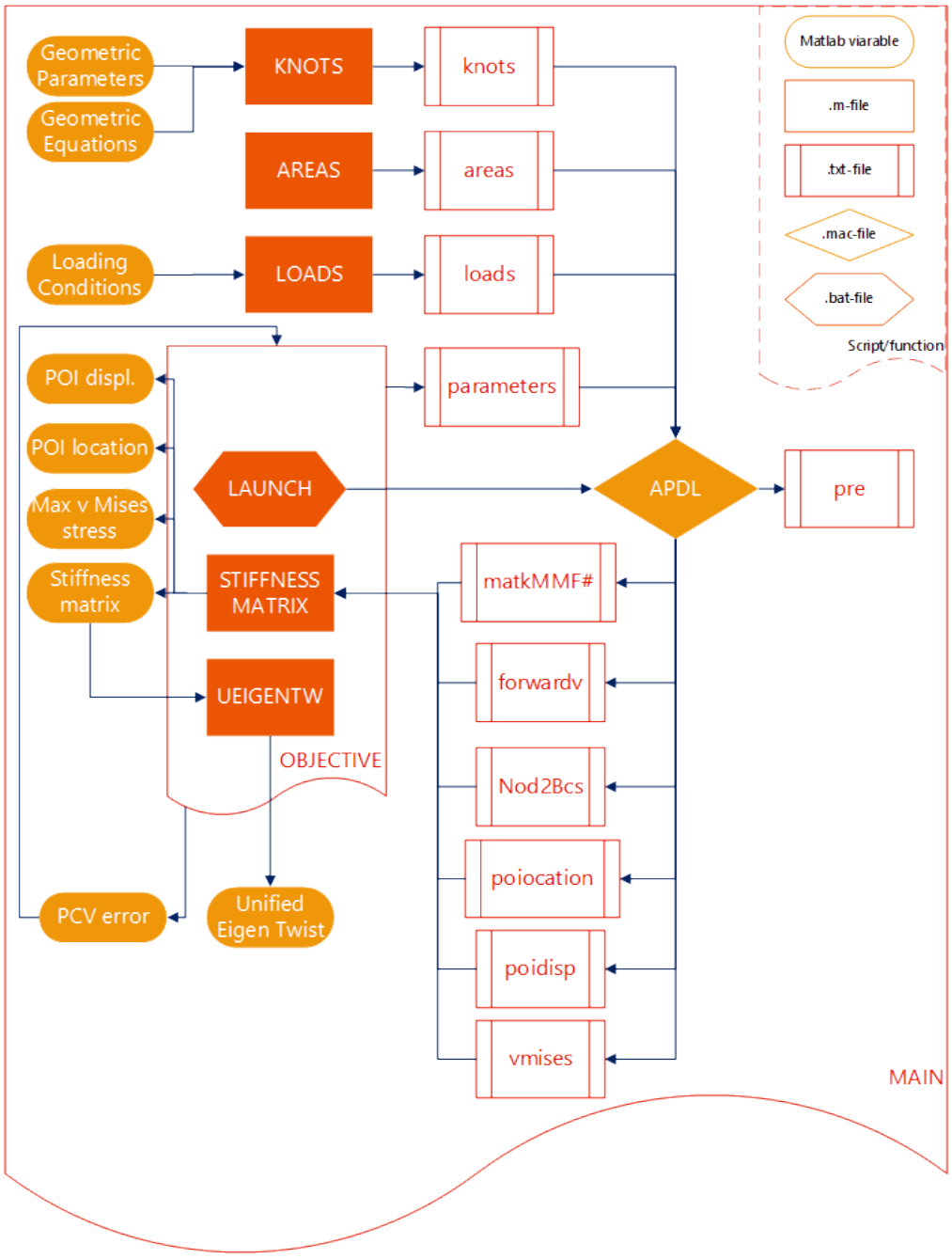

References/Further Readings

1. Bus Optimization:
   https://pdfs.semanticscholar.org/2ad8/225d5e386a428d19ac55a0dcb448f3e70796.pdf
2. Conference on Thin Walled Structures:
   https://www.ansys.com/-/media/ansys/corporate/resourcelibrary/conference-paper/2006-int-ansys-conf-22.pdf
3. Element Description:
   https://www.sharecnet.ca/Software/Ansys/en-us/help/ans_elem/Hlp_E_SHELL181.html
4. Modeling Shells:
   http://engr.bd.edu/davej/classes/met_415_3D02.html
5. Export Stiffness Matrix:
   http://www.ansystips.com/2017/export-stiffness-matrix-from-ansys.html
6. Degree of Freedom Ordering:
   https://www.sharcnet.ca/Software/Ansys/17.0/en-us/help/ans_apdl/apdldofordering.html

D

Measuring Stiffness Matrices with the UR5 Robot

This appendix discusses the main steps in evaluating large range of motion stiffness matrices of a shell mechanism with the Universal Robot, UR5. The selected general approach in evaluating the stiffness matrices is displacement based. The robot applies pure displacements and rotations in all 6 directions, a load-cell measures the resulting forces. These values combined construct the entire stiffness matrix at each evaluation point.

$$\begin{bmatrix} F_{xx} \\ F_{xy} \\ F_{xz} \\ T_{xrx} \\ T_{xry} \\ T_{xrz} \end{bmatrix} = \begin{bmatrix} {}^{F_{xx}}/_{dx} & \cdot & \cdot & \cdot & \cdot & \cdot \\ {}^{F_{xy}}/_{dx} & \cdot & \cdot & \cdot & \cdot & \cdot \\ {}^{F_{xz}}/_{dx} & \cdot & \cdot & \cdot & \cdot & \cdot \\ {}^{T_{xrx}}/_{dx} & \cdot & \cdot & \cdot & \cdot & \cdot \\ {}^{T_{xry}}/_{dx} & \cdot & \cdot & \cdot & \cdot & \cdot \\ {}^{T_{xrz}}/_{dx} & \cdot & \cdot & \cdot & \cdot & \cdot \end{bmatrix} \begin{bmatrix} dx \\ 0 \\ 0 \\ 0 \\ 0 \\ 0 \end{bmatrix} \tag{D.1}$$

The robot should deform the shell over the range of motion, and induce displacements to evaluate the stiffness matrix at pre-defined locations along that range of motion. Therefore, this appendix focuses on programming the robot so that it applies the desired displacements to the shell mechanism.

First we discuss the initialization of the robot. Second, we present a way of scripting the trajectory and small displacements. Finally, we elaborate on running a scripted code on the robot.

Initialization

In this stage we set up the starting point of the trajectory and align the robot's tool center point (TCP) to the origin of the load-cell, using the PolyScope user interface. The robot performs all linear movements relative to the TCP. For rotations it is important to align TCP and load-cell axes.

When programming in the Polyscope interface, one defines TCP location and orientation in the installation-tab (see Fig. D.1a). X, Y, and Z is the translation along the axes presented on the same screen. RX, RY, and RZ represent a rotation vector. The magnitude of this vector defines the rotation in radians. Make sure that the TCP is aligned with the load-cell origin, and the coordinate-system that defines POI trajectory.

Next, one should manually move the tool to the desired starting point and teach the robot to go here by adding that location as a waypoint of a *movel* or *movej* command. Starting point coordinates of the TCP are retrieved by going the the move-tab. After selecting base as feature, the screen (see Fig.D.1b) presents TCP coordinates and orientation belonging the current position. These coordinates are important for scripting TCP movement.

Scripting

For the robot to be able to read the script, it should have a *.script* file extension. This file contains linear movement commands *(movel(..))*, moving the TCP to a pose *(p[x,y,z,rx,ry,rz])*, and pause *(sleep(..))*

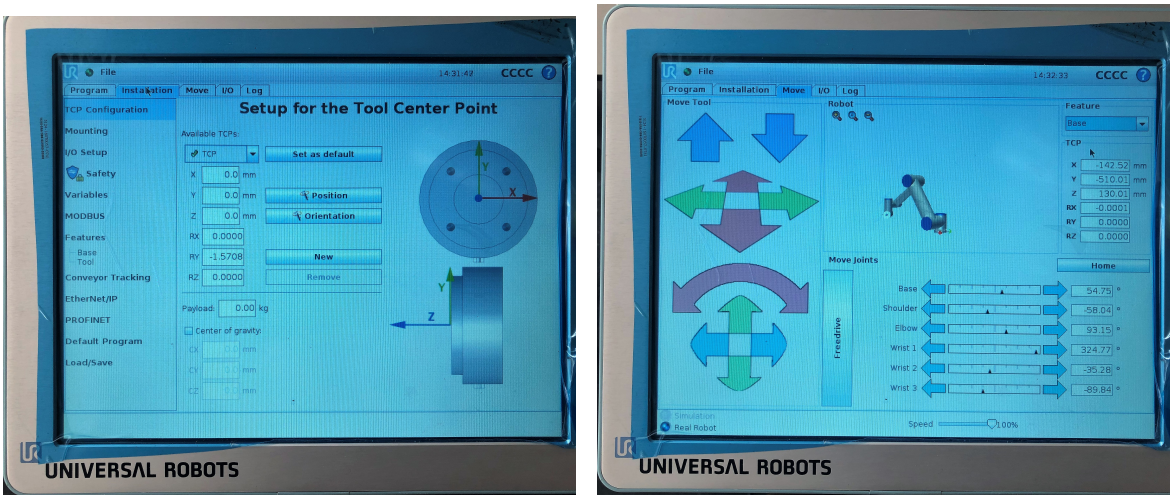

(a) (b)

Figure D.1: PolyScope screenshots to set up TCP and retrieve start point coordinates

commands. MatLab generates such a file based on the small displacement magnitudes, for evaluating the stiffness matrix, and computational evaluated POI displacements for the trajectory. These movements are relative to the starting point, following from the PolyScope user interface(Fig D.1b). An example MatLab script:

```
startingpoint = [-.14253, -.51, .13, 0, 0, 0];  % start coordinates from PolyScope
dx = [0.005, 0, 0, 0, 0, 0];                    % vector describing small x-displacement
...
drz = [0, 0, 0, 0, 0, 0.03];                    % vector describing small z-rotation

poidisp = [0 0 0 0 0 0;...                      % loadstep x 6 matrix describing ...
...                                             % evaluation points
0.0284 0 0.0353 0 0.3491 0];

fileID = fopen('sc4.script','w');               % write to .script file

for  i=1:loadstep                               % small perturbation loop
point = startingpoint+poidisp(i,:);             % calculate evaluation point
x = point + dx;                                 % calculate x-perturbation coordinate
...
rz = point + drz;

fprintf(fileID,'%s%f,%f,%f,%f,%f,%f%s\n','movel(p[',... % move linear to evaluation point
point(1),point(2),point(3),point(4),point(5),point(6),...
'], a=0.3, v=0.005)');                          % acceleration and speed
fprintf(fileID,'%s\n','sleep(2.0)');            % pause for two seconds

fprintf(fileID,'%s%f,%f,%f,%f,%f,%f%s\n','movel(p[',... % move linear to ...
x(1),x(2),x(3),x(4),x(5),x(6),...               % x-perturbation point
'], a=0.3, v=0.005)');
fprintf(fileID,'%s\n','sleep(1.0)');            % pause for one second
fprintf(fileID,'%s%f,%f,%f,%f,%f,%f%s\n','movel(p[',... % move linear back to ...
point(1),point(2),point(3),point(4),point(5),point(6),...%evaluation point
'], a=0.3, v=0.005)');
fprintf(fileID,'%s\n','sleep(1.0)');

...                                             % repeat for other directions
end

fclose(fileID);
```

Running a Script

One adds a script to the PolyScope program by going to the structure-tab and selecting *Script Code* (see Fig. D.2). In the command-tab of this script structure one selects *file* in the top right corner and clicks on edit (see Fig. D.2b). Next, one selects *open* and chooses the desired .script file on the flash drive. Finally, the script is added to the PolyScope program by clicking on save and exit (see Fig.D.2c).

(a) (b)

(c)

Figure D.2: PolyScope screenshots to set up TCP and retrieve start point coordinates

References/Further Readings

1. Universal Robots User Manual UR5/CB3:
   `https://www.universal-robots.com/download/`
2. Universal Robots The URScript Programming Language:
   `https://www.universal-robots.com/download/`
3. UR Script Script Programming from the Teaching Pendant:
   `http://www.zacobria.com/universal-robots-zacobria-forum-hints-tips-how-to/script-programming-from-the-teaching-pendant/`

Bibliography

[1] Ring, J., 2017. "Passive brace for the treatment of scoliosis utilizing compliant mechanisms". Master's thesis, Bucknell University.

[2] Miller, N. H., 1999. "Cause and natural history of adolescent idiopathic scoliosis.". *The Orthopedic clinics of North America,* **30**, July, pp. 343–52, vii.

[3] Weinstein, S. L., Dolan, L. A., Wright, J. G., and Dobbs, M. B., 2013. "Effects of bracing in adolescents with idiopathic scoliosis". *New England Journal of Medicine,* **369**(16), oct, pp. 1512–1521.

[4] Rigo, M., and Weiss, H.-R., 2008. "The chêneau concept of bracing–biomechanical aspects.". *Studies in health technology and informatics,* **135**, pp. 303–319.

[5] Rolton, D., Nnadi, C., and Fairbank, J., 2014. "Scoliosis: a review". *Paediatrics and Child Health,* **24**(5), may, pp. 197–203.

[6] Wynne, J. H., 2008. "The boston brace system philosophy, biomechanics, design & fit.". *Studies in health technology and informatics,* **135**, pp. 370–384.

[7] Nijenbanning, G., 1998. "Scoliosis redress. design of a force controlled orthosis". PhD thesis, 9.

[8] Park, J.-H., Stegall, P., and Agrawal, S. K., 2015. "Dynamic brace for correction of abnormal postures of the human spine". In 2015 IEEE International Conference on Robotics and Automation (ICRA), IEEE.

[9] Dries, T., 2018. "A biomechanical characterization of spinal motion data for the design of a compliant scoliosis brace". Master's thesis, TU Delft.

[10] Nijssen, J., 2017. "A type synthesis approach to compliant shell mechanisms". Master's thesis, TU Delft.

[11] Leemans, J., 2018. "Characterization of non-linear compliant shell mechanisms". Master's thesis, TU Delft.

[12] Bible, J. E., Biswas, D., Miller, C. P., Whang, P. G., and Grauer, J. N., 2010. "Normal functional range of motion of the lumbar spine during 15 activities of daily living". *Journal of Spinal Disorders & Techniques,* **23**(2), apr, pp. 106–112.

[13] Radaelli, G., and Herder, J., 2017. "Gravity balanced compliant shell mechanisms". *International Journal of Solids and Structures,* **118-119**, jul, pp. 78–88.

[14] Nijssen, J. P. A., Radaelli, G., Herder, J. L., Kim, C. J., and Ring, J. B., 2017. "Design and analysis of a shell mechanism based two-fold force controlled scoliosis brace". In Volume 5A: 41st Mechanisms and Robotics Conference, ASME.

[15] Leemans, J., Kim, C., van de Sande, W., and Herder, J., 2018. "Unified stiffness characterization of non-linear compliant shell mechanisms". *J. Mechanisms Robotics.*

[16] Lipkin, H Patterson, T., 1992. "Geometrical properties of modelled robot elasticity: Part i - decomposition". *DE-Vol. 45, Robotics, Spatial Mechanisms, and Mechanical Systems ASME 1992*.

[17] Ces edupack software, granta design limited, cambridge, uk, 2018 (www.grantadesign.com).

[18] Universal robots, user manual ur5/cb3.

[19] Ati industrial automation, f/t sensor: Mini40 https://www.ati-ia.com/products/ft/ft_models.aspx?id=Mini40.

[20] Richard S. Figliola, D. E. B., 2014. *Theory and Design for Mechanical Measurements*. WILEY.

[21] Kim, C. J., 2019. "On the geometry of stiffness and compliance under concatenation". In Proceedings of the ASME 2019 International Design Engineering Technical Conferences & Computers and Information in Engineering Conference IDETC/CIE 2019, ASME.

[22] Hatamizadeh, A., Song, Y., and Hopkins, J. B., 2018. "Optimizing the geometry of flexure system topologies using the boundary learning optimization tool". *Mathematical Problems in Engineering,* **2018**, pp. 1–14.

[23] Stacey, J. P., O'Donnell, M. P., and Schenk, M., 2018. "Thermal prestress in composite compliant shell mechanisms". In Volume 5A: 42nd Mechanisms and Robotics Conference, ASME.

[24] Desbiens-Blais, F., Clin, J., Parent, S., Labelle, H., and Aubin, C.-E., 2012. "New brace design combining CAD/CAM and biomechanical simulation for the treatment of adolescent idiopathic scoliosis". *Clinical Biomechanics,* **27**(10), dec, pp. 999–1005.